Journal of Computational Physics 257 (2014) 216–240

Contents lists available at ScienceDirect

Journal of Computational Physics

www.elsevier.com/locate/jcp

Phase field method to optimize dielectric devices for electromagnetic wave propagation

Akihiro Takezawa *, Mitsuru Kitamura

Division of Mechanical Systems and Applied Mechanics, Institute of Engineering, Hiroshima University, 1-4-1 Kagamiyama, Higashi-Hiroshima, Hiroshima, Japan

ARTICLE INFO

Article history:
Received 4 September 2012
Received in revised form 21 September 2013
Accepted 21 September 2013
Available online 2 October 2013

Keywords:
Phase field
Shape optimization
Electromagnetic system
Sensitivity analysis
Topology optimization
Level set

ABSTRACT

We discuss a phase field method for shape optimization in the context of electromagnetic wave propagation. The proposed method has the same functional capabilities as the level set method for shape optimization. The first advantage of the method is the simplicity of computation, since extra operations such as re-initialization of functions are not required. The second is compatibility with the topology optimization method due to the similar domain representation and the sensitivity analysis. Structural shapes are represented by the phase field function defined in the design domain, and this function is optimized by solving a time-dependent reaction diffusion equation. The artificial double-well potential function used in the equation is derived from sensitivity analysis. We study four types of 2D or 2.5D (axisymmetric) optimization problems. Two are the classical problems of photonic crystal design based on the Bloch theory and photonic crystal wave guide design, and two are the recent topics of designing dielectric left-handed metamaterials and dielectric ring resonators.

1. Introduction

Geometrical optimization has been studied to solve the problem of what shape is optimal in various problems. Recent development of optimization enables us to optimize geometry drastically, including topology. In recent studies, these methods have been used not only to optimize the existing structure but also generate a new shape having a specified function. These uses of optimization have contributed to the development of pure and applied physics (e.g. [1–10]). The contribution of geometrical optimization seems to be strongest for electromagnetic wave propagation, since research on finding geometry having new electromagnetic characteristics is active, as reviewed in [11].

Topology optimization is the most popular geometrical optimization method [12–14]. The basic idea is replacing the shape optimization problem by a two phase material distribution problem consisting of an original material and an ersatz material mimicking voids. With this formulation this method can generate holes for the target domain. However, since the original problem is ill-posed, homogenization is applied and the original problem is represented as a composite material optimization problem, namely, an optimization problem of a volume fraction of these materials. This representation raises the further problem of how to obtain clear shapes from the optimal density distribution [13,14].

Recently, the level set method for geometrical optimization [15–18] has been proposed to avoid the drawbacks described above. In this method, the target configuration is represented as a zero contour of the level set function, and the front moves along its normal direction according to the Hamilton–Jacobi equation. The moving direction of the front is decided by using shape sensitivity, which is used in classical shape optimization [19,20] as the velocity field for the Hamilton–Jacobi equation.

* Corresponding author. Tel.: +81 82 424 7544; fax: +81 82 422 7194.
E-mail addresses: akihiro@hiroshima-u.ac.jp (A. Takezawa), kitamura@naoe.hiroshima-u.ac.jp (M. Kitamura).

0021-9991/$ – see front matter
http://dx.doi.org/10.1016/j.jcp.2013.09.051

Level set methods allow topological changes (limited to eliminating holes), significantly improving structural performance. Moreover, this method is free from re-meshing, since the level set function is defined in an Eulerian coordinate system. The level set method was originally proposed by Osher and Sethian [21–23] as a numerical method for tracking free boundaries according to the mean curvature motion, and the mathematical background was subsequently clarified by several researchers [24–26]. The level set method has been applied to many optimization problems (e.g. [27–37]), including electromagnetic wave propagation.

As with the level set method, the phase field method is capable of handling the motion caused by domain states such as temperature and the motion caused by the domain shape, such as the mean curvature motion, and so can also be applied to geometrical optimization. The phase field method was developed as a way to represent the surface dynamics of phase transition phenomena such as solid–liquid transitions. Research on such physical modeling can be traced back to Cahn and Hilliard [38] and Allen and Cahn [39]. The mathematical fundamentals for these physical models were constructed by several researchers [40–42]. In the early stage of this research, contributions to computing actual phase transition phenomena were made by [43,44]. Outlines of the above history and methodologies can be found in several comprehensive reviews [45–47]. Bourdin and Chambolle [48] were the first to propose applying the phase field method to structural optimization, when it had initially been used to implement perimeter constraints [49,50]. After that, several useful structural optimization methods were developed that incorporate the phase field method (e.g. [51–54]).

Another shape optimization technique has been proposed using the phase field method for simulation with a moving boundary [55,56]. (Hereafter, when "phase field method" is used in the sense of shape optimization, it mentions this methodology.) This method has the almost same function as in the level set method, meaning it is a shape optimization based on a moving boundary accepting the topology change. This method has two advantages. The first is that it does not need to re-initialize the function as needs to be done in the conventional level set method. The second is that it is very compatible with topology optimization. The domain in the phase field method is represented by a density function, the same as in the topology optimization. The front motion is decided by the sensitivity with respect to the variable defined on the domain and not the boundary. Thus, despite the fact that the phase field method is basically a shape optimization method different from topology optimization, the sensitivity analysis framework developed by topology optimization can be applied to the phase field method. A disadvantage of the method is the thickness of the front domain corresponding to the actual boundary of the object. It must have a thickness including several grids to represent smooth motion of the boundary. This is not a serious problem in a 2D problem but cannot be overlooked in 3D problems.

Since above methods were mainly developed through linear elastic static and dynamic problems, another physical problem should be solved to confirm the utility of the methods. We choose electromagnetic wave propagation as the second target physical problem. First, the 2D method is a useful way to analyze a polarized in-plane wave device, especially in the field of photonics. Thus, the drawback of the phase field method with respect to 3D analysis is not serious. Second, optimization of the electromagnetic wave device is mainly done by topology optimization as mentioned at the start of the introduction. The phase field method can easily follow this analysis due to its compatibility with topology optimization. Moreover, few studies have been reported on using the phase field method to solve the electromagnetic problem.

In this research, we study the phase field method for shape optimization of electromagnetic wave propagation. First, we review the phase field method for shape optimization proposed in [55]. The structural shape is represented by the phase field function defined in the design domain containing the optimal configuration. The numerical computation is performed over the whole domain as the distribution optimization problem of two phase materials, as in conventional topology optimization. We optimize the phase field function by using a time-dependent reaction diffusion equation called the Allen–Cahn equation. An artificial double-well potential used in the equation is derived from sensitivity analysis to move the front in the direction decreasing the objective function. Then Maxwell's equations are used as the state equations. We explain the four types of 2D or 2.5D (axisymmetric) optimization problems in this paper. Two are classical topics, photonic crystal design based on the Bloch theory and photonic crystal wave guide design, and two are recent topics, design of dielectric left-handed metamaterials and dielectric ring resonators. We perform sensitivity analysis for each problem to construct the optimization procedure. The numerical results are finally shown for each problem to show the validity of the proposed method.

2. Phase field method for shape optimization

2.1. Phase field method

We define a phase field function $\phi(\boldsymbol{x})$ over an entire analysis domain to represent the phase of the local points therein, as shown in Fig. 1. From a physical point of view, the phase field function provides the average phase of the local points. Consider a closed system composed of two phases, one of which corresponds to the value α of the phase field function while the other corresponds to the value β ($\alpha < \beta$). We represent the boundary of each phase as a smooth function that interpolates the different values ϕ, which we term the "diffuse interface". The Van der Waals free energy of the system is given by

$$F(\phi) = \int_{\Omega} \left(\frac{\varepsilon^2}{2} |\nabla \phi|^2 + P(\phi) \right) dx, \tag{1}$$

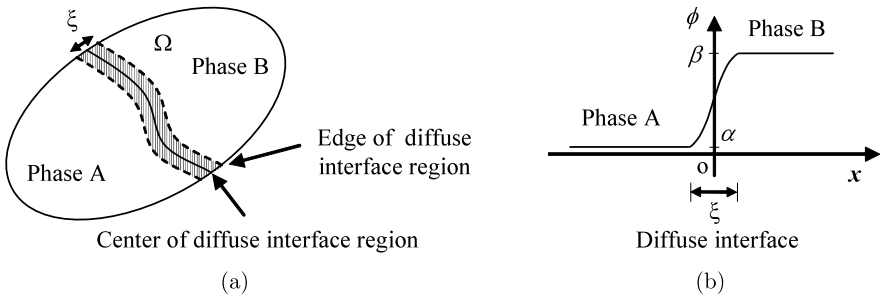

Fig. 1. Examples of the phase field function. (a) A 2D domain represented by the phase field function. (b) A 1D illustration of the phase field function.

where $\varepsilon > 0$ is a coefficient determining the effect of each term. The first term represents the interaction energy term of the field in mean field theory, and the second term represents a double well potential with the value $P'(\alpha) = P'(\beta) = 0$. The double well potential indicates that there are lower free energy values with minima corresponding to each phase.

Next, we consider the time-dependent evolution equation of the phase field function ϕ. The change of the phase field function with respect to time is assumed to be linearly dependent upon the direction in which the free energy function is minimized:

$$\frac{\partial \phi}{\partial t} = -K(\phi)\frac{\delta F(\phi)}{\delta \phi}, \tag{2}$$

where $K(\phi)$ is a variation rate function. Substituting Eq. (1) into Eq. (2), we obtain

$$\frac{\partial \phi}{\partial t} = K(\phi)\left(\varepsilon^2 \nabla^2 \phi - P'(\phi)\right). \tag{3}$$

Eq. (3) is known as the Allen–Cahn equation [39]. According to this equation, the front moves in its normal direction at a speed determined by the difference between each minimum of the double well potential $P(\phi)$ and the curvature of the diffuse interface as follows [57–59]:

$$v = s + \frac{1}{t}H + O\left(\frac{1}{t^2}\right), \quad t \gg 1, \tag{4}$$

where s is the speed due to the difference between each minimum of the double well potential $P(\phi)$, and H is the mean curvature of the diffuse interface. If the potential has equal minima, the motion is only governed by the mean curvature.

2.2. Domain representation of the target domain in the phase field method for shape optimization

We use a general shape optimization problem to explain the phase field method. Let Ω be the domain that varies during the optimization process, with the state of the domain Ω represented by some partial differential equations. The boundary $\partial\Omega$ of Ω is divided into two boundaries, a boundary $\partial\Omega_{\mathrm{D}}$ with Dirichlet boundary conditions and a boundary $\partial\Omega_{\mathrm{N}}$ with Neumann boundary conditions. The state variable $\boldsymbol{u}$ is calculated based on the state equations that have these boundary conditions. We introduce the extended design domain D that contains Ω. Here, a set of admissible shapes in D can be represented as

$$\mathcal{U}_{ad} = \left\{\Omega \subset D \;\middle|\; \Omega \in \mathbb{R}^d\right\}. \tag{5}$$

Thus, the shape optimization problem for Ω is defined as

$$\underset{\Omega \in \mathcal{U}_{ad}}{\text{minimize}}\; J(\Omega), \tag{6}$$

where $J(\Omega)$ is a functional with respect to state variable $\boldsymbol{u}$ whose value depends on the shape of Ω.

We represent the shapes of optimized domains using a phase field function as shown in Fig. 2. The phase field function $\phi(\boldsymbol{x})$ $(0 \leqslant \phi \leqslant 1)$ is defined in the domain D. We consider a setting where the domain Ω_1 $(\boldsymbol{x} \in D \mid \phi(\boldsymbol{x}) = 1)$ corresponds to the optimized shape Ω and the domain Ω_0 $(\boldsymbol{x} \in D \mid \phi(\boldsymbol{x}) = 0)$ corresponds to $D \setminus \Omega$. However, this setting is insufficient because a diffuse interface region exists when the phase field method is used. Let ξ represent the diffuse interface region. The domain representation of D is then formulated as

$$\begin{aligned} &\phi = 1 \iff \boldsymbol{x} \in \Omega_1, \\ &0 < \phi < 1 \iff \boldsymbol{x} \in \xi, \\ &\phi = 0 \iff \boldsymbol{x} \in \Omega_0, \end{aligned} \tag{7}$$

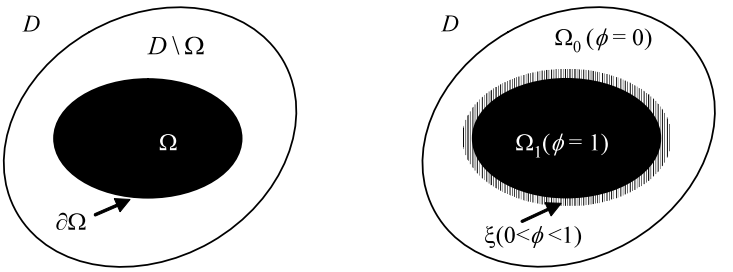

(a) An original domain (b) The domain represented by the phase field function

Fig. 2. The domain representation by the phase field function.

where

$$(\Omega_1 \cup \xi) \supset \Omega \quad \text{and} \quad (\Omega_0 \cup \xi) \supset D \setminus \Omega. \tag{8}$$

That is, the original domain Ω is represented as a subset of the union of Ω_1 and ξ. In the above setting, the position of the boundary $\partial\Omega$ is unclear except that it lies in ξ. However, as explained in Section 2, the diffuse interface region becomes very thin when ε is very small, in which case ξ can be regarded as approximately representing $\partial\Omega$. We can easily pick out a clear shape in a plot by choosing an arbitrary contour value such as $\phi = 0.5$ in the diffuse interface.

To achieve optimization of Ω in the phase field method, we consider the distribution of a physical property of the target domain as the design variable and clip the shape of the domain from the physical property distribution. Let us consider a domain with a phase field function ϕ defined over it, and the state $\boldsymbol{u}$ is dominated by a PDE having a term with coefficient $A(\phi)$ that is a function of ϕ. The three states Ω_1, Ω_0 and ξ are considered in this domain according to Eq. (7). Ω_1 is filled with a material whose physical property is $\boldsymbol{A}$, and Ω_0 is assumed to be filled with a material having a very small one that mimics a void to avoid singularities in the calculation. In addition, the material in the diffuse interface ξ has a virtual physical property using an interpolation function $E(\phi)$ defined in the range $E_{\min} \leqslant E(\phi) \leqslant E_{\max}$. Accordingly, we represent the distribution of the physical property E^* of the entire domain as

$$E^*(\phi) = \begin{cases} E_{\max}, & \text{if } \boldsymbol{x} \in \Omega_1, \\ E(\phi)\ (E_{\min} < E(\phi) < E_{\max}), & \text{if } \boldsymbol{x} \in \xi, \\ E_{\min}, & \text{if } \boldsymbol{x} \in \Omega_0. \end{cases} \tag{9}$$

2.3. Evolution of the phase field function

The phase field function evolves with a virtual time t in the interval $t_1 \leqslant t \leqslant t_2$, corresponding to a descent step of the function in the optimization problem. The evolution equation is formulated as

$$\begin{cases} \dfrac{\partial \phi}{\partial t} = \kappa \nabla^2 \phi - P'(\phi) & (t_1 \leqslant t \leqslant t_2), \\ \dfrac{\partial \phi}{\partial \boldsymbol{n}} = 0 & \text{on } \partial D, \end{cases} \tag{10}$$

where $\kappa = \varepsilon^2$ is a positive coefficient of the diffusion term and $P(\phi)$ is a double well potential. As explained in Section 2, when the phase field function follows Eq. (10), the diffuse interface moves in a normal direction with the velocity determined by the difference between the minima of the double well potential. The double well potential $P(\phi)$ is determined by sensitivity analysis to achieve motion in a direction that reduces the value of the objective function. The conditions that the double well potential $P(\phi)$ must satisfy are as follows:

$$P(0) = 0, \qquad P(1) = a J'(\phi_{t_1}), \qquad P'(0) = P'(1) = 0 \quad (a > 0), \tag{11}$$

where $J'(\phi)$ is the sensitivity of the objective function with respect to ϕ, ϕ_{t_1} is the value of ϕ at time t_1 and a is its positive coefficient. A sketch of the double well potential is shown in Fig. 3. Since the function evolves in the direction of the smaller minimum of the double well potential, the objective function can be minimized in the same way as for conventional steepest-descent methods.

Moreover, since the sensitivity distribution depends on the interpolation function $E(\phi)$ in Eq. (9), the boundary motion of the proposed methodology depends on the interpolation function the same way as with topology optimization.

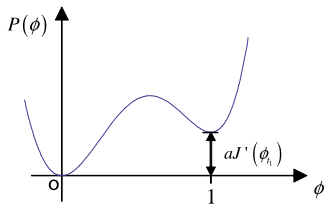

Fig. 3. Double well potential.

Note that some methods have been proposed that apply the perimeter minimization of the phase field method to perimeter control of topology optimization methods [48,51]. We remark that the primary difference between these methods and the proposed methodology is in their origin and functions. Since the aforementioned methods came from topology optimization, which updates the density function based on sensitivity analysis, nucleation of holes in the target structure is possible. Conversely, the proposed methodology aims for the same outcome using the level set method for shape optimization, whose roots are in classical shape optimization based on boundary variation. Thus, there are no hole nucleation mechanisms in our method. Because of this characteristic, the proposed methodology has an initial dependency unlike the topology optimization.

3. Phase field method for dielectric domain optimization in electromagnetic wave propagation

3.1. Domain representation

In the phase field method, the shape of the dielectric domain is represented as the distribution of the phase field function. The optimization is performed by representing the physical property as a function of the phase field function ϕ. The relative permittivity over the design domain ϵ is expressed as the function of the phase field function ϕ $(0 \leqslant \phi \leqslant 1)$ using the permittivity of the original dielectric material ϵ_1 and that of air ϵ_0 according to Eq. (9). The optimal shape of the dielectric domain can then be specified as a distribution in ϕ. Both ϵ_0 and ϵ_1 are assumed to be isotropic. The interpolation function used in the phase field interface is decided according to the target problem.

3.2. Equations of state

The 3D vector Helmholtz equations are the equations of state representing resonance-mode wave propagation within the dielectric domain with relative permittivity ϵ and the same permeability as that of open space. Assuming a time harmonic solution with angular frequency ω, we write the Helmholtz equation for the electric field $\boldsymbol{E}$ derived from Maxwell's equation as

$$\nabla \times (\nabla \times \boldsymbol{E}) + \epsilon \frac{\omega^2}{c^2} \boldsymbol{E} = 0, \tag{12}$$

where c is the speed of light. Conversely, the Helmholtz equation for the magnetic field $\boldsymbol{H}$ is written as

$$\nabla \times \left(\frac{1}{\epsilon} \nabla \times \boldsymbol{H} \right) + \frac{\omega^2}{c^2} \boldsymbol{H} = 0. \tag{13}$$

$\boldsymbol{H}$ and $\boldsymbol{E}$ can be calculated from the following Maxwell–Ampère equation without the current density term:

$$\nabla \times \boldsymbol{H} = \epsilon \frac{\partial \boldsymbol{E}}{\partial t}. \tag{14}$$

The following boundary conditions are introduced for the domain governed by the above equations depending on the target problem. We show only the formulations with respect to the electric field are shown here. By replacing $\boldsymbol{E}$ by $\boldsymbol{H}$, we can applied them to the magnetic field.

$$\text{Floquet periodic boundary condition:} \quad \boldsymbol{E} = \boldsymbol{E}_{\mathrm{src}} e^{-j\boldsymbol{k}\cdot\boldsymbol{r}_{\mathrm{per}}} \quad \text{on } \Gamma_{\mathrm{pe}}, \tag{15}$$

$$\text{First-order absorbing boundary condition:} \quad \boldsymbol{n} \times (\nabla \times \boldsymbol{E}) + ik\boldsymbol{n} \times (\boldsymbol{n} \times \boldsymbol{E}) = 0 \quad \text{on } \Gamma_{\mathrm{ab}}, \tag{16}$$

$$\text{First-order absorbing boundary with incident wave:} \quad \boldsymbol{n} \times (\nabla \times \boldsymbol{E}) + ik\boldsymbol{n} \times (\boldsymbol{n} \times \boldsymbol{E}) = -2ik\boldsymbol{n} \times (\boldsymbol{n} \times \boldsymbol{E}_{\mathrm{inc}}), \tag{17}$$

$$\text{Perfect electric (magnetic) wall:} \quad \boldsymbol{E} \times \boldsymbol{n} = 0 \quad \text{on } \Gamma_{\mathrm{pw}}, \tag{18}$$

where $\boldsymbol{E}_{\mathrm{src}}$ is the electric field vector on the source boundary in the periodic boundary condition, $\boldsymbol{k}$ is the wave number vector with respect to the coordinate system, $\boldsymbol{r}_{\mathrm{per}}$ is a vector perpendicular to the periodic boundaries with a magnitude equal to the distance between them, $\boldsymbol{n}$ is the unit vector normal to the boundary, k is the wave number in free-space and $\boldsymbol{E}_{\mathrm{inc}}$ is the incident electric field vector.

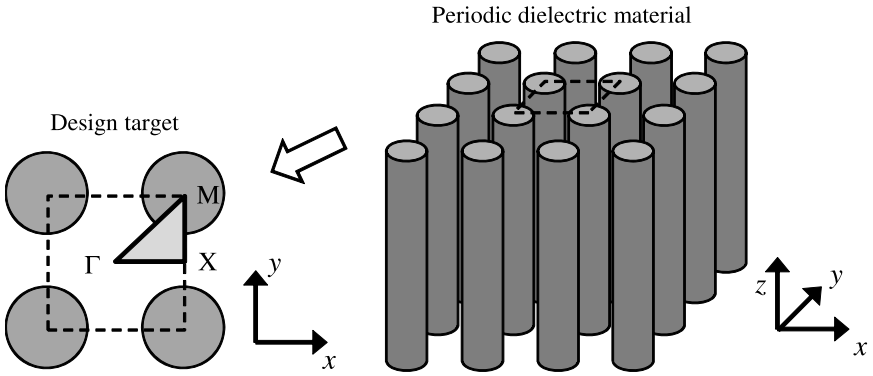

Fig. 4. An outline of a 2D photonic crystal composed of dielectric columns homogeneous along the z direction and its unit cell. The triangle in the unit cell represents the Brillouin zone.

3.3. Optimization problems

We now apply the optimization method to designing photonic crystal unit cells, photonic crystal wave guides, dielectric left-handed metamaterials (LHMs) and dielectric ring resonators.

3.3.1. Design of photonic crystal

Our first case study is designing the unit cell of a 2D photonic crystal [60], which is the classical problem in designing dielectric devices for electromagnetic wave propagation first discussed in [61]. In this problem, we consider periodic structures that extend along the z direction as shown in Fig. 4. The shape of a unit cell on the xy plane is designed to prevent light propagation from all directions in a certain frequency range. We limit the target wave to a transverse-magnetic (TM) wave with an electric field only in the z direction and a magnetic field only in the xy plane ($\boldsymbol{E} = [0, 0, E_z]^T$, $\boldsymbol{H} = [H_x, H_y, 0]^T$). We assume that the square unit cell has the mirror symmetrical shape on the horizontal center line, vertical center line and diagonal center line. Due to the symmetry, the wave vectors $\boldsymbol{k}$ are considered on only the irreducible Brillouin zone [60] shown in Fig. 4. The design domain is also set to this zone. That is, the distribution of the dielectric material is optimized there, and the resulting shape is repeated in other areas of the unit cell.

The photonic band gap is calculated as the gap between the upper and the lower eigenfrequencies of the target order in every possible $\boldsymbol{k}$ in the irreducible Brillouin zone. The calculation is performed by solving the Helmholtz equation in Eq. (12) only for E_z as the eigenvalue problem under the Floquet periodic boundary condition in Eq. (15) on 2D domain. We evaluate the performance of the photonic crystal using the absolute difference between the two dimensionless frequencies formulated as $(\omega_{\text{target}+1} - \omega_{\text{target}})d/2\pi c$ [1,4], where ω_{target} and $\omega_{\text{target}+1}$ represent the lower and upper angular eigenfrequencies of the optimized gap and d is the length of the unit cell. (On the other hand, the band gap is evaluated as a relative value by dividing the gap by the sum of the maximum value of the lower frequency and the minimum value of the upper frequency in [5].) Thus, we define the objective function for photonic crystal design as maximizing the gap between the eigenvalues $\Lambda = \omega^2$. The optimization is formulated as the following unconstrained problem:

$$\text{minimize } J_1(\phi) = -\left[\min\left\{\Lambda_{\text{target}+1}(\phi, \boldsymbol{k})\right\} - \max\left\{\Lambda_{\text{target}}(\phi, \boldsymbol{k})\right\}\right]. \tag{19}$$

This objective function contains the effects minimizing the maximum value of the target order eigenvalue and maximizing the minimum value of the target + 1 order eigenvalue independently of the existence of the gap. Thus, if there is no gap in the target structure, the optimization decreases the "band crossing" represented as a positive objective function. After the objective function becomes zero, which means the band crossing is zero, the objective function becomes negative and the band is generated. *Note that the described objective function works for cases where the upper band lies above the lower band for all k-values, that is, where the target and target + 1 order eigenvalues can be distinguished. If not, numerical techniques are required to specify these eigenvalues.*

3.3.2. Design of photonic crystal wave guide

Second, we study design optimization of the photonic crystal wave guide. The design domain is set to the corner of the L-shaped photonic crystal wave guide as shown in Fig. 5. This problem was also studied in the early stage of electromagnetic wave propagation optimization [2]. In this problem, we optimize the distribution of the dielectric material for the target wave, which is limited to a TM wave as in the first example. The calculation is performed by solving the Helmholtz equation in Eq. (12) only for E_z as a frequency response problem for the input wave in a 2D domain. For designing photonic crystal wave guides, we use the integrated time-averaged Poynting vector in the specified domain for the objective func-

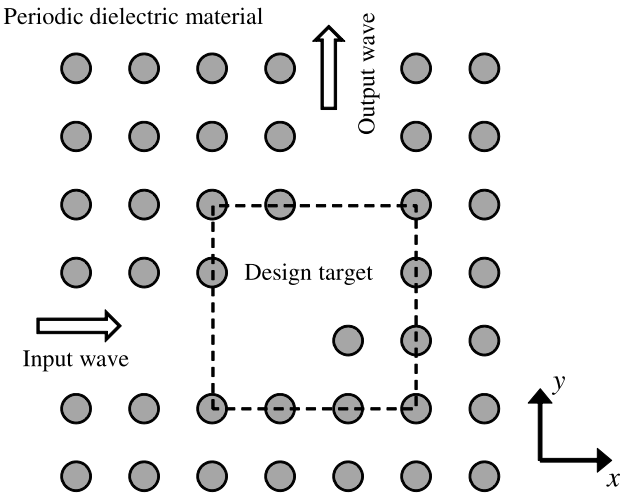

Fig. 5. An outline of a 2D photonic crystal waveguide composed of dielectric columns homogeneous along the z direction.

tion. By summing the Poynting vector corresponding to several frequencies in the optimization, the optimization problem is formulated as the unconstrained problem

$$\text{minimize } J_2(\phi) = \sum_m^i \hat{J}_{2i}(\phi) = \sum_m^i \int_D C_1(\boldsymbol{x}) \mathrm{Re}(\boldsymbol{E}_i \times \bar{\boldsymbol{H}}_i)\, dx, \tag{20}$$

where m represents the number of frequencies considered in the optimization, $\boldsymbol{E}_i$ and $\boldsymbol{H}_i$ are the electric and magnetic fields corresponding to the i-th input frequencies, $C_1(\boldsymbol{x})$ is a coefficient function denoting the location of the target domain and the component of the Poynting vector, $\mathrm{Re}(\cdot)$ and $\mathrm{Im}(\cdot)$ represent respectively the real and imaginary parts of the variable and the bar expresses the conjugate.

3.3.3. Design of dielectric left-handed metamaterials

As a case study dealing with a recent topic in optimizing electromagnetic wave propagation, we consider the design of a dielectric 2D LHM with negative permeability studied in [62]. Dielectric LHMs have an advantage over conventional ones using metallic split-ring resonators or thin wires in terms of avoiding metallic loss and wider effective frequency regions. The LH behavior can be observed in periodic dielectric media as shown in Fig. 4. A Mie resonance mode occurring at a certain frequency provides the LH characteristic for periodic media (e.g. [63–65]). In this problem, the wave is a transverse-electric (TE) wave with a magnetic field only in the z direction and electric field only in the xy plane ($\boldsymbol{E} = [E_z, E_y, 0]^T$, $\boldsymbol{H} = [0, 0, H_z]^T$). We analyze the device with the unit cell model considering periodicity. The Helmholtz equation for the magnetic field $\boldsymbol{H}$ simplified to a TE wave is solved on the domain as a frequency response problem for a wave incident from the left. The right side is considered as an output side. We set a first-order absorbing boundary condition to both the input and output sides. A perfect electric wall is set to the upper and the lower sides to represent the periodicity. To evaluate the performance of the LHM, we use the following effective permeability [66] formulated by the S-parameters:

$$\mu_{\mathrm{eff}} = n_{\mathrm{eff}} Z_{\mathrm{eff}}, \tag{21}$$

where

$$n_{\mathrm{eff}} = \frac{1}{kd} \cos^{-1}\left\{ \frac{1}{S_{21}} \left(1 - {S_{11}}^2 + {S_{21}}^2\right) \right\}, \tag{22}$$

$$Z_{\mathrm{eff}} = \sqrt{\frac{(1+S_{11})^2 - {S_{21}}^2}{(1-S_{11})^2 - {S_{21}}^2}}, \tag{23}$$

and k is the wave number, d is the length of a unit cell, n_{eff} is the effective refractive index and Z_{eff} is the effective impedance. S_{11} and S_{21} are S-parameters formulated as

$$S_{11} = \frac{\int_{\Gamma_{\mathrm{in}}} (\boldsymbol{E} - \boldsymbol{E}_1^{\mathrm{inc}}) \cdot \boldsymbol{E}_1^{\mathrm{inc}}\, ds}{\int_{\Gamma_{\mathrm{in}}} |\boldsymbol{E}_1^{\mathrm{inc}}|^2\, ds}, \tag{24}$$

$$S_{21} = \frac{\int_{\Gamma_{\mathrm{out}}} \boldsymbol{E} \cdot \boldsymbol{E}_2^{\mathrm{sc}}\, ds}{\int_{\Gamma_{\mathrm{out}}} |\boldsymbol{E}_2^{\mathrm{sc}}|^2\, ds}, \tag{25}$$

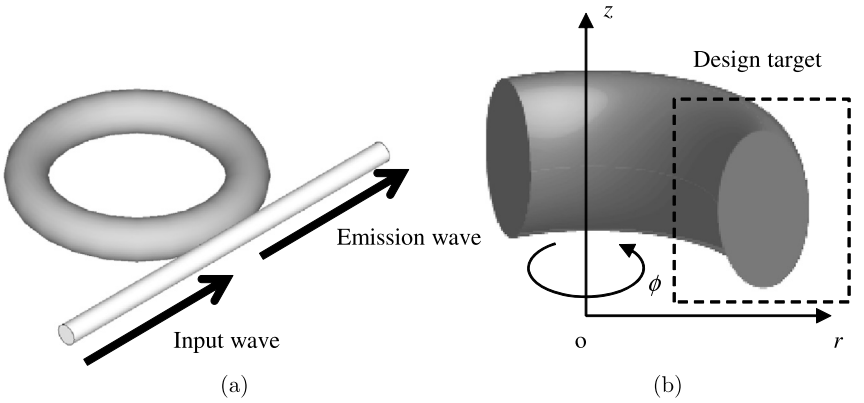

Fig. 6. (a) An outline of a dielectric ring resonator. (b) The analysis and design domain in cylindrical coordinates.

where Γ_{in} and Γ_{out} are the input and output boundaries of the wave corresponding to ports 1 and 2 respectively, and $\boldsymbol{E}_1^{\text{inc}}$ and $\boldsymbol{E}_2^{\text{sc}}$ are incident and scattering electric fields on the input and output boundaries respectively. The objective function is formulated to make the real or imaginary part of the effective permeability by minimizing each as follows:

$$\text{minimize } J_3(\phi) = \text{Re}(\mu_{\text{eff}}) \quad \text{or} \quad \text{Im}(\mu_{\text{eff}}). \tag{26}$$

3.3.4. Design of dielectric ring resonator

The above three design problems are performed in a 2D domain. As a 2.5D (axisymmetric) design problem, we perform the cross-sectional design of dielectric ring resonators in a cylindrical coordinate system studied in [67]. The optical modes, set up in these devices by emissions from input light, form circular continuous closed beams governed by internal reflections along the boundary of the resonator as shown in Fig. 6(a). The mode shape with the circular electric field distribution is called a whispering-gallery (WG) mode. This type of resonator has potential applications to low-threshold micro-cavity lasers and light-matter systems for quantum networking [68–70]. Optical resonators exploiting WG modes have attained high performance levels such as high quality factor (Q factor), which measures the inverse of the energy decay rate, and low mode volume, which signifies the spatial confinement of the light [69].

In this problem, TM waves are considered as emissions. We use cylindrical coordinates to model a WG ring resonator centered on the origin in free space as illustrated in Fig. 6(b). The coordinate system consists of the axial, azimuthal, and radial coordinates. We treat the vertical cross-sectional device shape in the z–r plane as the design target and obtain the final axisymmetric form by generating the solid of revolution. The Helmholtz equation for the magnetic field $\boldsymbol{H}$ is solved as an eigenvalue problem in the cylindrical coordinate system. To suppress spurious modes in the analysis, we introduce a weak penalty term [71] to yield the following modified equation used in [72]:

$$\nabla \times \left(\frac{1}{\epsilon} \nabla \times \boldsymbol{H} \right) - p \nabla (\nabla \cdot \boldsymbol{H}) + \frac{\omega^2}{c^2} \boldsymbol{H} = 0, \tag{27}$$

where p is a coefficient. The first term describes perfect magnetic conduction and the latter term first-order absorption on the boundary. The state variable is the set comprising the time-dependent radial, azimuthal, and axial components of the magnetic field vector $\boldsymbol{H}(\boldsymbol{r}, t)$. We factorize the azimuthal dependence from the variable to obtain

$$\boldsymbol{H}(\boldsymbol{r}) = e^{iM\phi} \left[H_r(r,z), iH_\phi(r,z), H_z(r,z) \right]^T, \tag{28}$$

where M is the azimuthal mode order.

The performance criteria in designing a WG ring resonator are the Q factor and mode volume. In calculating the Q factor, we consider only the radiation loss, for which Q_{rad} is calculated as follows [69,73]:

$$\text{Q}_{\text{rad}} = \frac{\text{Re}(f)}{2\,\text{Im}(f)}. \tag{29}$$

In the analysis for the domain surrounded by the perfect matched layer (PML) domain, the real part of the frequency represents the total energy of the domain, whereas the imaginary part represents the rate of energy absorption by the PML domain, *i.e.* the radiation loss (Chapter 5 in [74]).

In addition, the mode volume is formulated as [69,73]

$$\text{V}_{\text{mode}} = \frac{\int_D \epsilon |\boldsymbol{E}|^2 \, dx}{\max(\epsilon |\boldsymbol{E}|^2)}. \tag{30}$$

During optimization, we target the following three tasks:

1. Maximizing the Q factor associated with emissions as expressed by Eq. (29).
2. Minimizing the mode volume as expressed by Eq. (30).
3. Specifying the emission wavelength $\lambda = c/\mathrm{Re}(f)$.

We first fulfill task 3 by introducing the corresponding equality constraint. Assuming normalized eigenmodes $\boldsymbol{H}$ ($\int_D |\boldsymbol{H}|^2\,dx = 1$) in the eigenfrequency analysis, the total electric energy over the analysis domain equals the square of the angular eigenfrequency ($\int_D \epsilon |\boldsymbol{E}|^2\,dx = \mathrm{Re}(\omega)^2$) [75,76]. That is, by pre-specifying the emission wavelength and azimuthal mode order, both numerators in the expressions for the Q factor and mode volume are constant during optimization. Thus, the objective functions for Task 1, J_{Q}, and Task 2, J_{V}, and the equality constraint h for Task 3 are formulated as

$$\underset{\phi}{\text{minimize}}\ J_{\mathrm{Q}}(\phi) = \mathrm{Im}(f), \tag{31}$$

or

$$\underset{\phi}{\text{minimize}}\ J_{\mathrm{V}}(\phi) = -\max\left(\epsilon |\boldsymbol{E}|^2\right), \tag{32}$$

subject to

$$h(\phi) = \lambda - \lambda_0 = 0, \tag{33}$$

with λ_0 denoting the specified wavelength.

3.4. Sensitivity analysis

The gap of the double well potential $P(\phi)$ is set based on sensitivity analysis of the objective function with respect to ϕ, which is the function defined on D. Here, we show only the results of the sensitivity analysis and explain the detailed derivation in Appendix A. The sensitivity of the i-th eigenvalue Λ_i used in the objective function in Eq. (19) is given by

$$\Lambda_i'(\phi) = -\epsilon'(\phi)\frac{\Lambda_i}{c^2}\boldsymbol{E}_i \cdot \boldsymbol{E}_i, \tag{34}$$

where $\boldsymbol{E}_i$ is the i-th eigenvector. As explained in Appendix A, the sensitivity of the eigenvalue can be calculated without adjoint variables.

Note that, when the eigenvalue is repeated, it is not differentiable in the normal sense. In this case, only directional derivatives can be obtained [77,78].

The sensitivity of the Poynting vector in the specified domain in Eq. (20) is calculated as

$$\hat{J}_2'(\phi) = -\epsilon'(\phi)\frac{\omega^2}{c^2}\boldsymbol{E} \cdot \boldsymbol{p}, \tag{35}$$

where $\boldsymbol{p}$ is the adjoint variable calculated from the following adjoint equations:

$$\int_D C_1 \cdot \frac{1}{2}\mathrm{Re}\left\{\boldsymbol{v} \times \overline{\left(-\frac{1}{j\omega\mu}\nabla \times \boldsymbol{E}\right)} + \boldsymbol{E} \times \overline{\left(-\frac{1}{j\omega\mu}\nabla \times \boldsymbol{v}\right)}\right\} dx$$
$$+ \int_D (\nabla \times \boldsymbol{v}) \cdot (\nabla \times \boldsymbol{p})\,dx - \int_D \epsilon(\phi)\frac{\omega^2}{c^2}\boldsymbol{v} \cdot \boldsymbol{p}\,dx - \int_\Gamma \boldsymbol{n} \cdot \left\{\boldsymbol{v} \times (\nabla \times \boldsymbol{p})\right\} ds = 0, \tag{36}$$

$$\boldsymbol{n} \times \nabla \times \boldsymbol{p} + ik\boldsymbol{n} \times \boldsymbol{n} \times \boldsymbol{p} = 0 \quad \text{on } \Gamma_{\mathrm{ab}} \text{ and } \Gamma_{\mathrm{inc}}. \tag{37}$$

The sensitivity of the S-parameters used in calculating the effective permeability in Eq. (21) is calculated with

$$S_{11}'(\phi) = -\frac{1}{\int_{\Gamma_{\mathrm{in}}} |\boldsymbol{E}_1^{\mathrm{inc}}|^2\,ds}(\nabla \times \boldsymbol{H}) \cdot \left(\frac{\epsilon'(\phi)}{\epsilon^2}\nabla \times \boldsymbol{H}\right), \tag{38}$$

$$S_{12}'(\phi) = -(\nabla \times \boldsymbol{p}) \cdot \left(\frac{\epsilon'(\phi)}{\epsilon^2}\nabla \times \boldsymbol{H}\right), \tag{39}$$

where $\boldsymbol{p}$ is the adjoint variable calculated from the adjoint equations

$$\frac{1}{\int_{\Gamma_{\rm out}} |\boldsymbol{E}_2^{\rm sc}|^2\,ds}\int_{\Gamma_{\rm out}} \boldsymbol{v}\cdot\boldsymbol{E}_2^{\rm sc}\,ds+\int_D (\nabla\times\boldsymbol{v})\cdot(\nabla\times\boldsymbol{p})\,dx-\int_D \epsilon(\phi)\frac{\omega^2}{c^2}\boldsymbol{v}\cdot\boldsymbol{p}\,dx-\int_\Gamma \boldsymbol{n}\cdot\left\{\boldsymbol{v}\times(\nabla\times\boldsymbol{p})\right\}ds=0, \tag{40}$$

$$\boldsymbol{n}\times\nabla\times\boldsymbol{p}+ik\boldsymbol{n}\times\boldsymbol{n}\times\boldsymbol{p}=0 \quad \text{on } \Gamma_{\rm in} \text{ and } \Gamma_{\rm out}, \tag{41}$$

$$\left(-\frac{1}{j\omega\mu}\nabla\times\boldsymbol{p}\right)\times\boldsymbol{n}=0 \quad \text{on } \Gamma_{\rm pw}. \tag{42}$$

In the case of the ring resonator design problem, the sensitivity of the eigenfrequency is required in Eq. (31), which is calculated from the sensitivity of the i-th eigenvalue Λ_i given by

$$\Lambda_i'(\phi)=-(\nabla\times\boldsymbol{H}_i)\cdot\left(\frac{\epsilon'(\phi)}{\epsilon^2}\nabla\times\boldsymbol{H}_i\right). \tag{43}$$

The maximum local energy density used in the objective function in Eq. (32) is calculated by using a function $C_2(\boldsymbol{x})$ having the value 1 at the maximum energy point and the value 0 at other points:

$$\frac{\partial\max(\epsilon|\boldsymbol{E}|^2)}{\partial\phi}=\frac{\partial C_2(\boldsymbol{x})\epsilon|\boldsymbol{E}_i|^2}{\partial\phi}=\frac{\partial C_2(\boldsymbol{x})\mu|\boldsymbol{H}_i|^2}{\partial\phi}. \tag{44}$$

Thus, its sensitivity is obtained as

$$\frac{\partial\max(\epsilon|\boldsymbol{E}_i|^2)}{\partial\phi}=-\int_D(\nabla\times\boldsymbol{p})\cdot\left(\frac{\epsilon'(\phi)}{\epsilon^2}\nabla\times\boldsymbol{H}_i\right), \tag{45}$$

where $\boldsymbol{p}$ is the adjoint variable calculated from the following adjoint equations

$$\int_D C_2(\boldsymbol{x})\boldsymbol{v}\cdot\boldsymbol{p}\,dx-\int_D(\nabla\times\boldsymbol{v})\cdot\left(\frac{1}{\epsilon}\nabla\times\boldsymbol{p}\right)dx$$
$$-\int_D\frac{\Lambda_i}{c^2}\boldsymbol{v}\cdot\boldsymbol{p}\,dx-\int_D p(\nabla\cdot\boldsymbol{p})(\nabla\cdot\boldsymbol{v})\,dx-\int_\Gamma\boldsymbol{n}\cdot\left\{\boldsymbol{v}\times(\nabla\times\boldsymbol{p})\right\}ds=0, \tag{46}$$

$$\boldsymbol{n}\times\nabla\times\boldsymbol{p}+ik\boldsymbol{n}\times\boldsymbol{n}\times\boldsymbol{p}=0 \quad \text{on } \Gamma_{\rm ab}. \tag{47}$$

4. Numerical implementation

4.1. Algorithm

Based on the above formulation, the optimization algorithm is constructed as follows.

1. Set the initial value of the phase field function ϕ expressing the initial shape of domain Ω.
2. Iterate the following procedure until convergence.
   (a) Calculate the state variable $\boldsymbol{u}$ and adjoint state $\boldsymbol{p}$ with respect to ϕ_n at the n-th iteration by solving the state equation and the adjoint equation using the finite element method.
   (b) Calculate the objective function and constraints.
   (c) Calculate the sensitivity of the objective function and prepare the evolution equation for ϕ.
   (d) Calculate the updated value of ϕ by solving the evolution equation.
3. Obtain the optimal shape of Ω expressed as the optimal distribution of ϕ.

4.2. Setting the evolution equation

We set the double well potential satisfying Eq. (11). We set it to be

$$P(\phi)=W(\boldsymbol{x})w(\phi)+G(\boldsymbol{x})g(\phi), \tag{48}$$

where

$$w(\phi)=\phi^2\left(1-\phi^2\right),\qquad g(\phi)=\phi^3\left(6\phi^2-15\phi+10\right), \tag{49}$$

which are the same as those used in [79]. $w(\phi)$ is a function satisfying $w(0)=w(1)=w'(0)=w'(1)=0$, and $g(\phi)$ is one with $g(0)=0$, $g(1)=1$ and $g'(0)=g'(1)=0$. Sketches of these functions are shown in Fig. 7. $W(\boldsymbol{x})$ and $G(\boldsymbol{x})$ are coefficients of these functions. $W(\boldsymbol{x})$ determines the height of the wall of the double well potential, which affects the thickness of the diffuse interface. $W(\boldsymbol{x})$ is set to be $\frac{1}{4}$ here. The value of $G(\boldsymbol{x})$ is chosen to be $G(\boldsymbol{x})=aJ'(\phi_{t_1})$ as explained

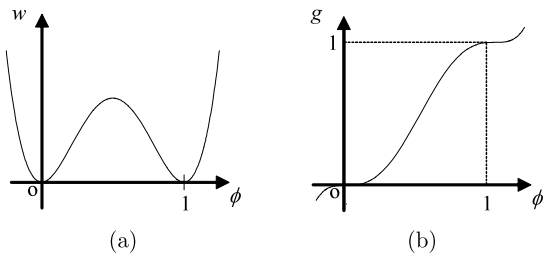

Fig. 7. Sketches of functions (a) w and (b) g.

Section 2.3. To avoid complicated parameter settings due to the order difference of $J'(\phi)$ depending on the optimization problem, we first normalize the sensitivity by dividing by its L^2-norm, and the new coefficient η is set as

$$G(\boldsymbol{x}) = \eta \frac{J'(\phi_{t_1})}{\|J'(\phi_{t_1})\|}. \tag{50}$$

Substituting Eqs. (48)–(50) into Eq. (10), we obtain

$$\begin{aligned}\frac{\partial \phi}{\partial t} &= \kappa \nabla^2 \phi - \frac{\partial}{\partial \phi}\big(W(\boldsymbol{x}) w(\phi) + G(\boldsymbol{x}) g(\phi)\big) \\ &= \kappa \nabla^2 \phi - \left(\frac{1}{4} w'(\phi) + \eta \frac{J'(\phi_{t_1})}{\|J'(\phi_{t_1})\|} g'(\phi)\right) \\ &= \kappa \nabla^2 \phi + \phi(1-\phi)\left\{\phi - \frac{1}{2} - 30\eta \frac{J'(\phi_{t_1})}{\|J'(\phi_{t_1})\|}(1-\phi)\phi\right\} \quad (t_1 \leqslant t \leqslant t_2).\end{aligned} \tag{51}$$

4.3. Numerical method for the evolution equation

The finite difference method is used to solve Eq. (51) numerically. We discretize the time derivative term using the forward Euler scheme and solve the equation with the explicit scheme. The time step Δt is restricted by the following Courant–Friedrichs–Lewy (CFL) condition for stable convergence in the 2D case:

$$\kappa\left(\frac{\Delta t}{(\Delta x)^2} + \frac{\Delta t}{(\Delta y)^2}\right) \leqslant \frac{1}{2}, \tag{52}$$

where $\Delta t > 0$ is the time step and Δx and Δy are space steps in the x and y directions respectively.

Aside from the above CFL condition, we must consider the convergence of the reaction term. Here, the reaction term is discretized by a so-called semi-implicit scheme [79], in which forward time terms are partly included. In the 2D case, let $\phi^n_{i,j}$ be the value of ϕ at the n-th iteration at the point $\boldsymbol{x}_{i,j}$. The scheme then leads to the following discretization:

$$\begin{aligned}\frac{\phi^{n+1}_{i,j} - \phi^n_{i,j}}{\Delta t} &= \kappa\left(\frac{\phi^n_{i-1,j} - 2\phi^n_{i,j} + \phi^n_{i+1,j}}{(\Delta x)^2} + \frac{\phi^n_{i,j-1} - 2\phi^n_{i,j} + \phi^n_{i,j+1}}{(\Delta y)^2}\right) \\ &\quad + \begin{cases} \phi^{n+1}_{i,j}(1-\phi^n_{i,j}) r(\phi^n_{i,j}) & \text{for } r(\phi^n_{i,j}) \leqslant 0, \\ \phi^n_{i,j}(1-\phi^{n+1}_{i,j}) r(\phi^n_{i,j}) & \text{for } r(\phi^n_{i,j}) > 0, \end{cases}\end{aligned} \tag{53}$$

where

$$r(\phi^n_{i,j}) = \phi^n_{i,j} - \frac{1}{2} - 30\eta \frac{J'(\phi_{t_1})}{\|J'(\phi_{t_1})\|} \phi^n_{i,j}(1-\phi^n_{i,j}). \tag{54}$$

This discretization guarantees that ϕ remains in the interval $0 \leqslant \phi \leqslant 1$ even when the time step is large. Although the forward time term ϕ^{n+1} is included in the right side of the above equation, ϕ^{n+1} can obviously be calculated easily without solving a linear system, and the computational cost is almost equal to that for the ordinary explicit scheme.

4.4. Handling of equality constraint

Normally, we use the sensitivity in Eq. (50) to choose the double well potential gap that decides the moving direction of the phase field interface. This way, the constraint is embedded in the objective function using the Lagrange multiplier method [18]. However, when handling equality constraints like Eq. (33), the solution of Eq. (51) oscillates around the limit of the equality constraint and does not converge easily to the optimal solution. Here, as a special numerical technique for

handling the equality constraint, we decide the potential gap based on sequential linear programing (SLP). SLP is one of the simplest methods that can handle the equality constraint problem directory. Let us consider the minimization of the objective function $J(\boldsymbol{X})$ with an equality constraint $h(\boldsymbol{X})=0$ with respect to a design variable vector $\boldsymbol{X}=[X_1, X_2, \ldots, X_n]$. In SLP, the increment $\Delta\boldsymbol{X}$ of the design variable $\boldsymbol{X}$ is obtained as the solution of the following linear programming problem:

$$\text{minimize } J(\boldsymbol{X}) + \nabla J(\boldsymbol{X})^T \Delta\boldsymbol{X}, \tag{55}$$

subject to

$$h(\boldsymbol{X}) + \nabla h(\boldsymbol{X})^T \Delta\boldsymbol{X} = 0, \tag{56}$$

$$\Delta X_{\text{low}} \leqslant \Delta X_i \leqslant \Delta X_{\text{up}} \quad \text{for } i = 1, \ldots, n, \tag{57}$$

where ΔX_{low} and ΔX_{up} are the lower and upper bounds of ΔX_i and the upper suffix ^{T} denotes the transpose.

It is only in designing dielectric ring resonators that the above linear programming problem is solved in each optimization iteration using the discretized phase field function as the design variable, and the obtained increment is used to form the double well potential gap. Note that in this method the obtained increment of the phase field function works only on the phase field interface. Thus, unlike the ordinary SLP method, the equality constraint might not always be satisfied, although this method worked well in the numerical example of this study.

5. Numerical examples

To confirm the validity of the proposed method, we study the four numerical examples described in Section 3. In all examples, we regard a material representing a void as air with relative permittivity $\epsilon_0 = 1$. We ignore the frequency dependence of the relative permittivity of the dielectric material. The relative permeabilities of the both air and the dielectric material are set to 1. The coefficient of normalized sensitivity η in Eq. (50) is set to 20. At each iteration, we perform a finite element analysis of the state equation and one update of the evolution equation for the phase field function by solving the finite difference equation of the semi-implicit scheme. The time step Δt is set to be 0.9 times the limit of the Courant number. All optimal configurations are plotted as the distribution of the phase field function of the optimal results. All finite element analyses are performed with a commercial software, COMSOL Multiphysics, using the second-order Lagrange element. The design domain is discretized by the square element that is used for both finite element and finite difference analyses. We set the evaluation point of the phase field function on the center of the square element. Let the grid interval of the finite difference mesh be l. The diffusion coefficient κ in Eq. (51) is based on the value $0.1 \times l^2$.

5.1. Design of photonic crystal

We perform the first optimization for designing the unit cell of a photonic crystal. One unit cell is modeled with the finite element method. The length d of the unit cell is set to 1 as a dimensionless parameter. Since we assume mirror symmetries in the unit cell, we only regard the area shown in Fig. 8 as the design domain, and resulting configurations are copied to other areas on the unit cell. In the design domain, the relative permittivity is formulated as a function of the phase field:

$$\epsilon(\phi) = \left\{ \frac{1}{\epsilon_0} + \phi\left(\frac{1}{\epsilon_1} - \frac{1}{\epsilon_0} \right) \right\}^{-1}. \tag{58}$$

The relative permittivity ϵ_1 of the dielectric material is set to 8.9 (alumina). The unit cell domain is meshed with 100×100 square elements. The diffusion coefficient κ is set to $0.5 \times l^2$. We calculate the wave vector $\boldsymbol{k}$ of the Floquet periodic boundary condition in Eq. (15) in the triangular irreducible Brillouin zone, with a step size of 0.05. We maximize the band gap above the first-, second- and third-order eigenfrequencies. The initial shape and the corresponding dispersion diagram are shown in Fig. 8. The initial shape does not have any band gaps in the depicted frequency range.

Because the first and second eigenvalues and the first, second and third eigenvalues are repeated at points X and M respectively in the initial shape, we calculated all possible directional derivatives and accepted the best one for updating the density function at the first iteration to identify target eigenvalues. Fig. 9 shows the convergence histories of the objective functions until convergence with 50 iterations. The variation of the objective function from negative to positive indicates generation of the band gap through the first few optimization iterations. Fig. 10(a), (c) and (e) shows the 3×3 array of the optimal configuration of the unit cell of the last iteration for the three cases. Fig. 10(b), (d) and (f) shows the calculated dispersion diagram for the shape. Each dispersion diagram shows the dimensionless frequency $\omega d/2\pi c$. The band gaps were certainly obtained above the specified eigenfrequency, although the optimization started with no band gap shape. The optimal configuration for the first band gap is nearly 0.2 circle radius, which is the reference shape in [60]. The optimal configurations of the second and third band gaps were also similar to the one proposed by [4], although the size of each part is different because of the difference in permittivity of the dielectric material. These comparisons also confirm the validity of the proposed method. The increases in the objective function after extracting black and white shapes are 0.84%, 0.60% and 1.83%. These values show the modeling error caused by the shape representation of the field function.

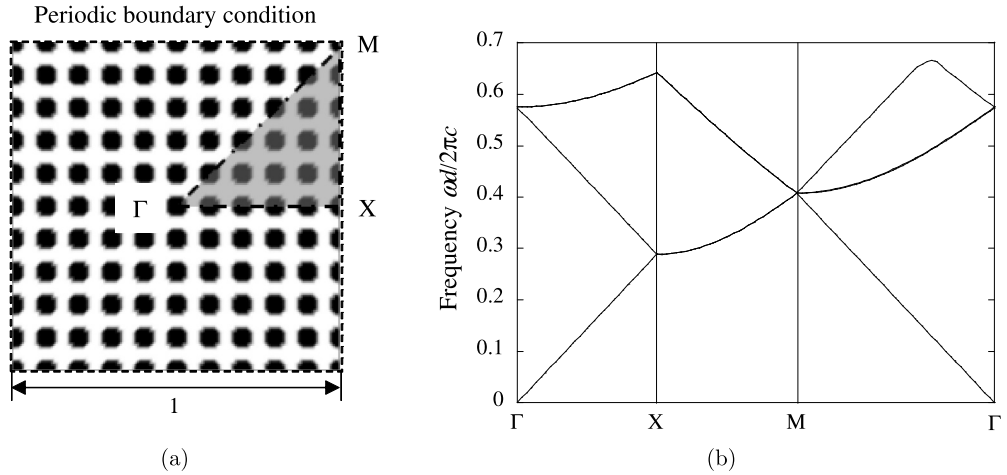

Fig. 8. (a) Initial shape for the photonic crystal design problem. The inset triangle shows the irreducible Brillouin zone and the design domain. (b) The dispersion diagram of the initial shape.

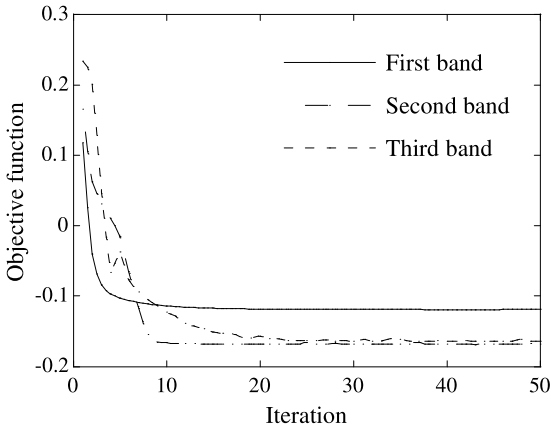

Fig. 9. Convergence history of the objective function of the photonic crystal optimization.

Fortunately, our optimization did not encounter any eigenvalue crossing problem [80] around the target band gap order in any examples studied. However, it could occur depending on the initial shape. One way to overcome this is introducing a so-called mode tracking technique (e.g. [80]).

5.2. Design of photonic crystal wave guide

For the second optimization we design the shape of the corner part of a photonic crystal wave guide. The analysis domain is shown in Fig. 11. The dielectric material is located periodically over the domain, and the wave guide is constructed by removing it according to the intended wave path. The length d of the unit cell is 0.57 μm. The incident wave enters from the port on the left bottom side, and the output port is set on the upper right side. The design domain is set on the corner of the wave guide. We use the upper right part of the domain as the reference domain for evaluating the Poynting vector. In the design domain, we formulate the relative permittivity the same way as in the previous example using Eq. (58). We set the relative permittivity ϵ_1 of the dielectric material to 11.4 (GaAs). The design domain is meshed with 200×200 square elements. Other domains are meshed with triangular elements. The diffusion coefficient κ is set to $0.2 \times l^2$.

Since the preferred range of the dimensionless frequencies $\omega d/2\pi c$ is from 0.35 to 0.42 for this wave guide [60], those of the incident waves are set to 0.38, 0.39 and 0.40 as a middle range. We set the electric field of the incident wave to the constant value 1 on the boundary. The initial shapes are set to two types as shown in Fig. 12 considering the initial dependency of the proposed method. The first is a periodic dielectric material, which does not propagate the wave. The second is the reference shape reported in [60], which directs wave propagation in the specified range.

Fig. 13 shows convergence histories of objective functions until 50 iterations. Fig. 14 shows optimal configurations after 41 iterations from the initial shape shown in Fig. 12(a) and 44 iterations from the initial shape shown in Fig. 12(b). The objective functions calculated from Fig. 14(a) and (b) are -3.35×10^{-16} W and -3.36×10^{-16} W (2.8% improvement from the reference shape), which are similar results. Although the optimization started from the shape that does not direct

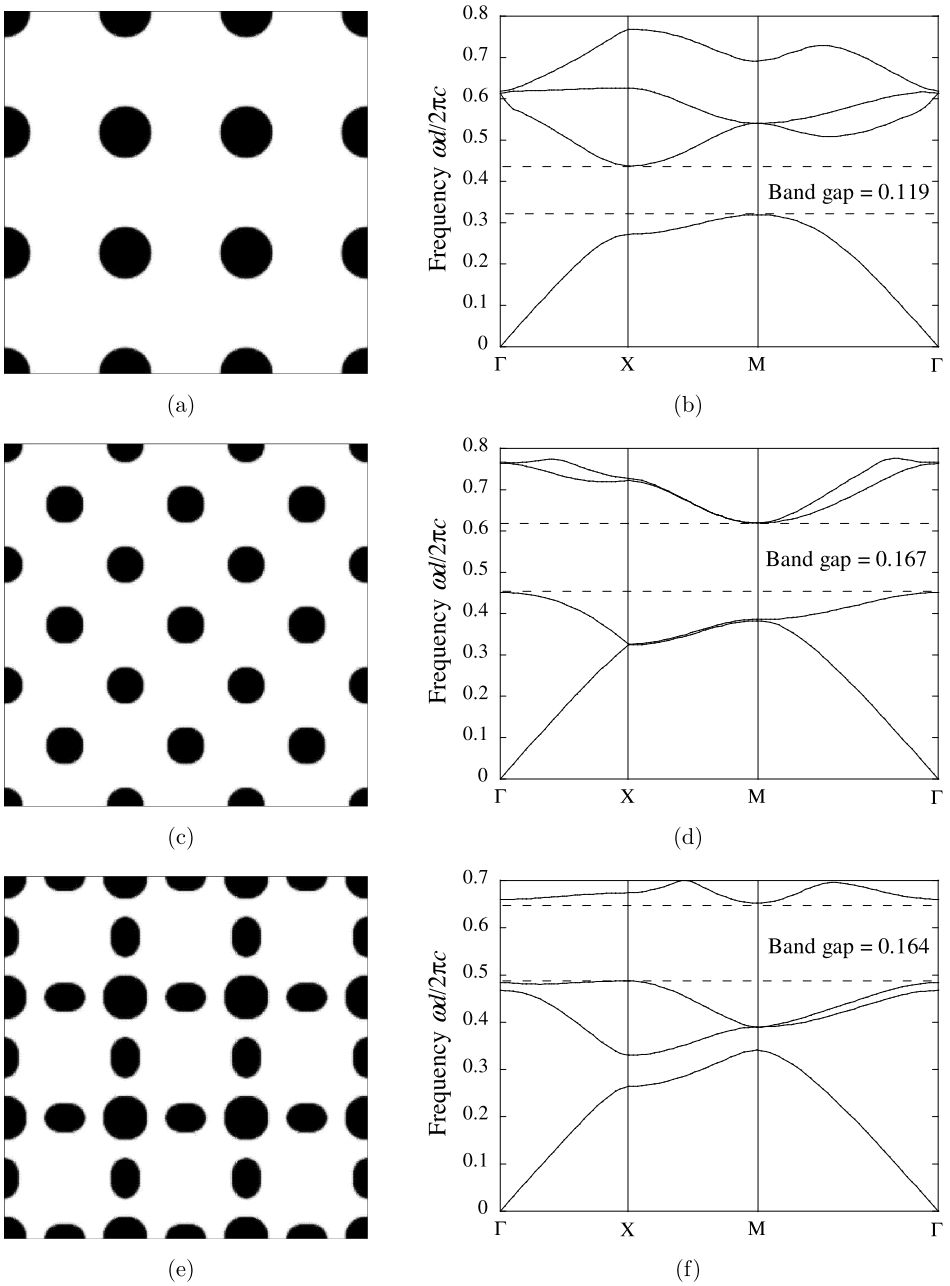

Fig. 10. Optimal configurations and dispersion diagrams. (a) and (b) First band. (c) and (d) Second band. (e) and (f) Third band.

wave propagation, the optimal shapes that propagate the wave with the specified frequency were obtained in Fig. 14(a). Fig. 15 shows the electric field distribution for the incident wave with the dimensionless frequency 0.39 in both optimal configurations. We observed a smooth bending of the electric field in both cases. Fig. 16 shows the integrated Poynting vector in the reference domain when the dimensionless frequency of the incident wave is from 0.35 to 0.42. Both shapes achieve slightly higher values than the reference shape in the middle frequency range from 0.38 to 0.40. The changes in the objective function after extracting black and white shapes are 0.30% and 0.60%.

5.3. Design of dielectric left-handed metamaterial

For the third optimization we design a dielectric LHM. The design target is assumed to be a periodic arrangement of dielectric poles as in the first example. The analysis domain is set as a square unit cell including the inner square design domain shown in Fig. 17. The length d of the unit cell is 120 μm. Assuming mirror symmetry along the x and y axes, the

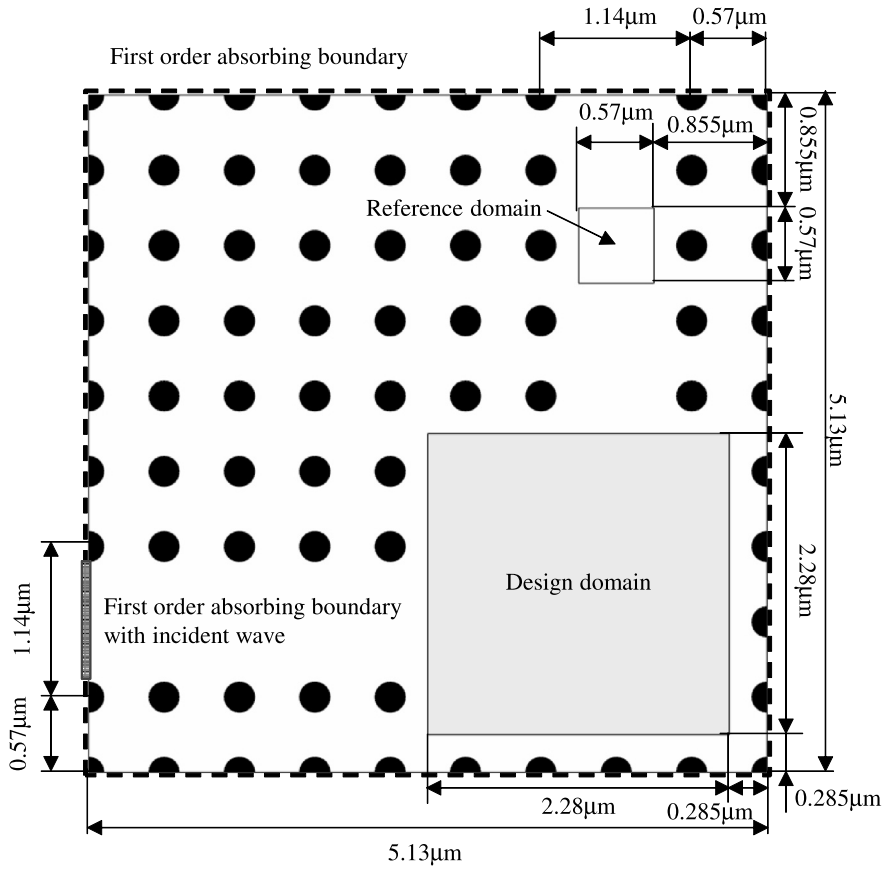

Fig. 11. Analysis domain for designing the photonic crystal wave guide including the design domain.

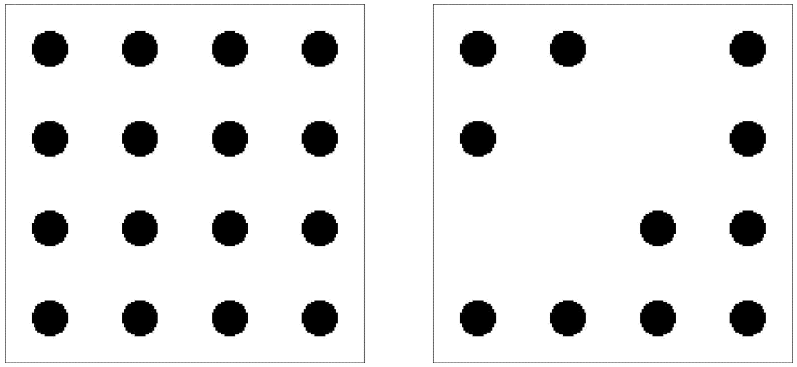

Fig. 12. Two initial shapes for designing the photonic crystal wave guide. (a) Periodic dielectric materials. (b) Reference shape.

optimization is performed on the upper right side of the design domain. We set the length of the design domain to 80 μm. To represent the periodicity along the y direction, we set a perfect electric wall at the top and bottom sides of the domain. Both sides are given a first-order absorbing boundary with a wave incident on the left side and scattered to the right side along the x direction. We formulate the relative permittivity in the design domain as

$$\epsilon(\phi) = \epsilon_0 + \phi(\epsilon_1 - \epsilon_0). \tag{59}$$

The relative permittivity ϵ_1 of the dielectric material is set to $100 - i$ as a virtual material including a little loss for the numerical stability as done in [62]. The analysis domain is meshed with 120×120 square elements. The electric field of the incident wave is set to the constant value 1 on the boundary. We set the target frequency, which we use as the frequency

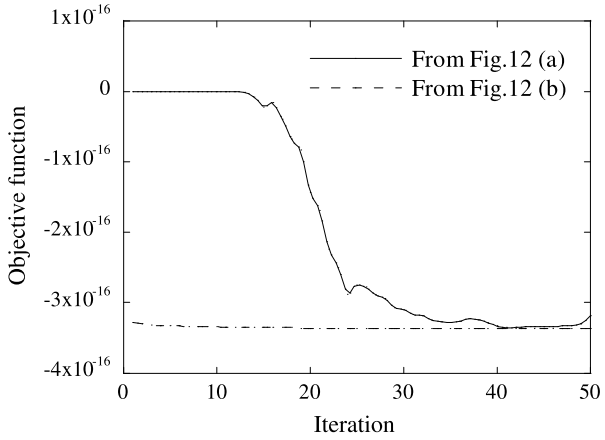

Fig. 13. Convergence history of the objective function of the photonic crystal wave guide optimization.

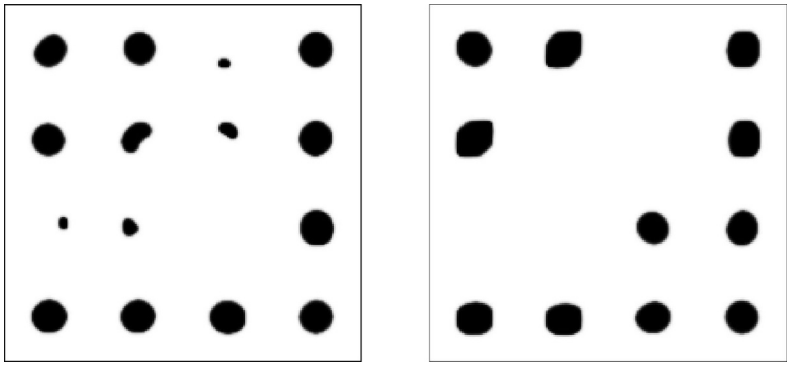

Fig. 14. Optimal configurations for the photonic crystal wave guide. (a) From initial shapes shown in Fig. 12(a). (b) From initial shapes shown in Fig. 12(b).

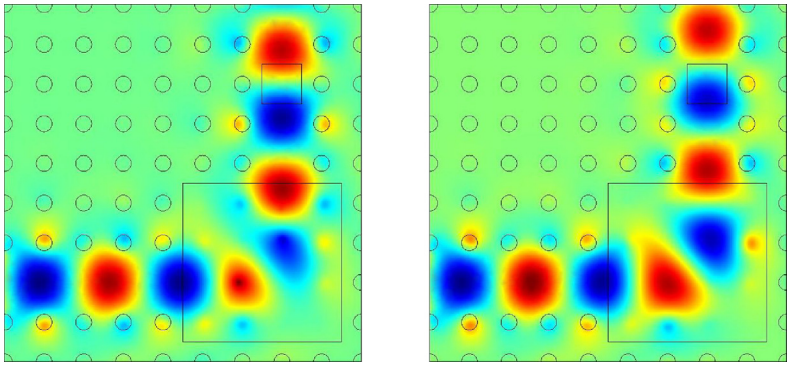

Fig. 15. Electric field distribution with the incident wave with dimensionless frequency 0.39. (a) Optimal configuration shown in Fig. 14(a). (b) Optimal configuration shown in Fig. 14(b).

of the incident wave, to 0.3 THz. The initial shape is set to a 60 μm diameter circle. The diffusion coefficient κ is set to $0.1 \times l^2$. We first minimize the imaginary part of the effective permeability. Then, we optimize the real part.

Fig. 18 shows convergence histories of the real and imaginary part of the effective permeability. We performed 94 and 16 iterations for the imaginary and real part optimizations respectively. Fig. 19 shows the optimal configurations for the imaginary and real parts of the effective permeability. These results are similar to those obtained in [62]. Fig. 20 shows the magnetic field distributions and electric field directions in these optimal configurations. Fig. 21 shows the effective permeability for both configurations obtained by varying the frequency of the input wave from 0.2 THz to 0.5 THz. The imaginary and real parts of the effective permeability take the negative peaks at the specified frequency. So-called Mie

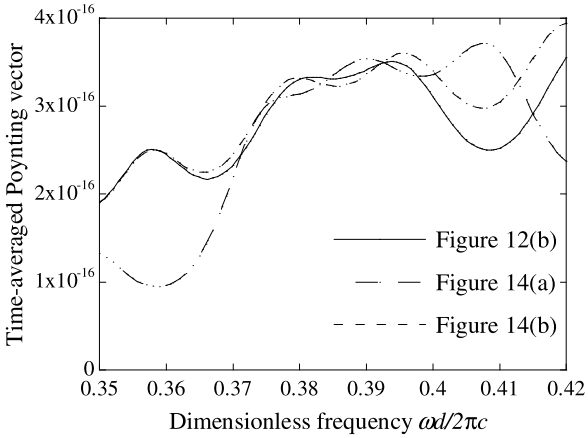

Fig. 16. Integrated Poynting vectors in the reference domain of the optimal and reference configurations.

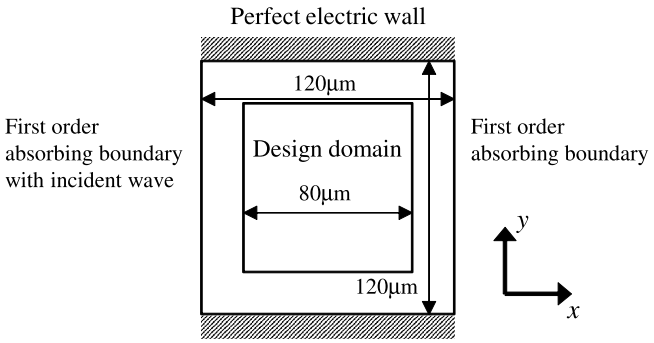

Fig. 17. Analysis model for designing the dielectric LHM including the design domain.

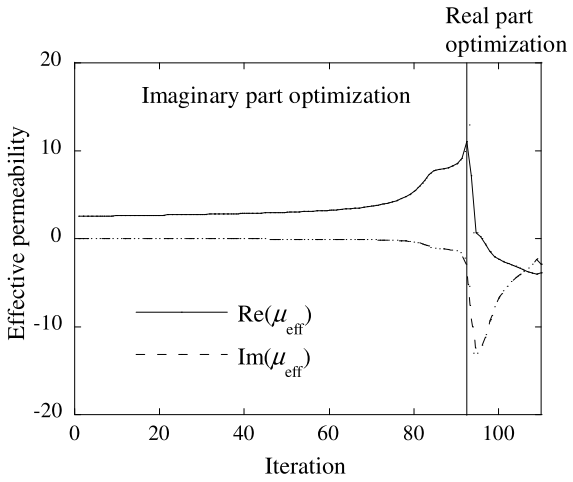

Fig. 18. Convergence history of the effective permeability of the dielectric metamaterial optimization.

resonance modes are observed in Fig. 20(c) and (d), which has a localized distribution of the magnetic field on the center of the dielectric material. This is the main mode for the dielectric LHM. We see in Fig. 20(a) and (b) that although the hot spot of the magnetic field is slightly off the center of the dielectric material after we optimize the imaginary part, the hot spot is exactly in the center after we optimize the real part. The change in the objective function after extracting black and white shapes is 1.85%.

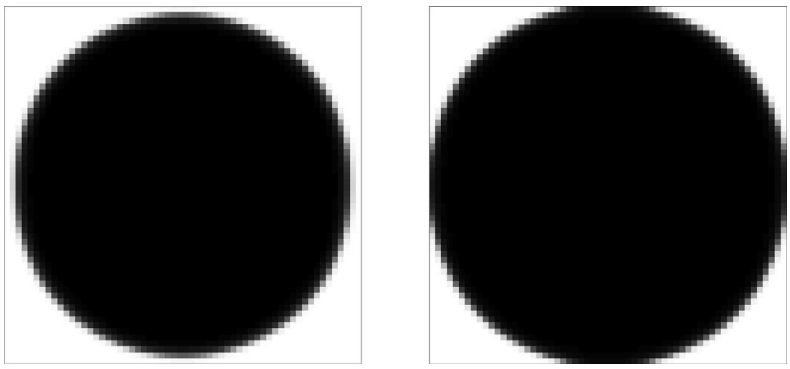

Fig. 19. Optimal configurations obtained after optimizing (a) the imaginary part and (b) the real part of the effective permittivity.

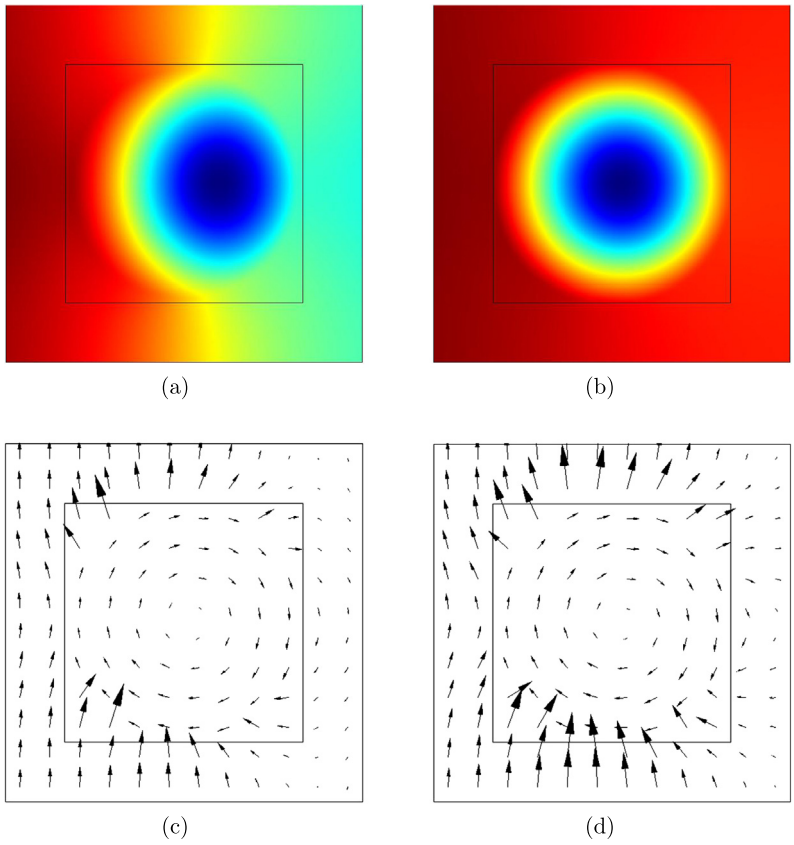

Fig. 20. Distribution of magnetic field and arrows indicating the direction of the electric field for the 0.3-THz incident wave. (a) and (c) are results from the optimal configuration shown in Fig. 19(a). (b) and (d) are results from the optimal configuration shown in Fig. 19.

5.4. Design of dielectric ring resonator

As our final numerical example, we optimize a dielectric ring resonator. To perform iterating numerical optimization based on the finite element method, we need the target WG eigenmode to be automatically selected from the numerous resulting eigenmodes. We introduce the two-step analysis proposed in [72] to specify the target mode during the iteration using the analysis domains shown in Fig. 22. First, we solve the small closed finite-element model composed of a device surrounded by a perfect magnetic wall, as drawn in Fig. 22(a), to obtain the eigenfrequency of the target WG mode. The first eigenmode of the model corresponds to the target WG mode. Second, we solve for the original model surrounded by PML domains, as drawn in Fig. 22(b), specifying the target eigenfrequency obtained by the closed model.

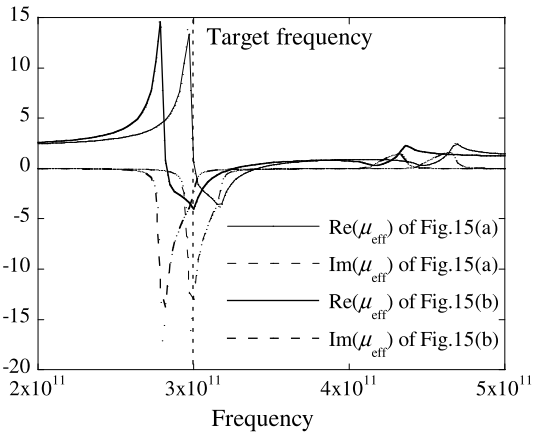

Fig. 21. Effective permeability of the optimal configurations with an incident wave from 0.2 to 0.5 THz.

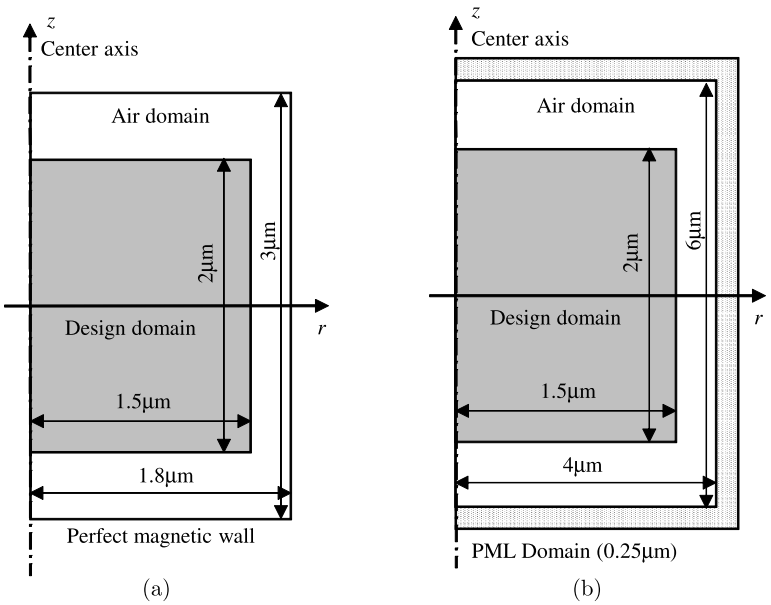

Fig. 22. Analysis domain for designing the dielectric ring resonator including the design domain. (a) Closed model only used for finding the frequency corresponding to the target WG mode. (b) Open model used for the optimization.

In the design domain, the relative permittivity is formulated the same way as in the third example using Eq. (59). Optimizations are performed with specified TM modes ($p = 1$, $M = 11$). The design domain is meshed with 75×100 square elements. The other domains are meshed with triangular elements. The diffusion coefficient κ is set to $0.1 \times l^2$. Assuming horizontal mirror symmetry of the optimal shapes, we only optimize the upper half of the design domain. Thus, the 3750 design variables are updated during optimization. The medium constituting the resonator is assumed to be GaAlAs with $\epsilon_1 = 11.28$. We maximize the Q factor and minimize the mode volume V using Eqs. (31) and (32), respectively. The phase field function is updated by using the SLP based method of Eqs. (55)–(57) to handle the equality constraint directory. The initial shape for both optimizations is shown in Fig. 23. We chose it for the ease of mode volume optimization since its initial dependency is stronger than that of the Q factor optimization because Eq. (32) handles the local maximum energy.

Fig. 24 shows convergence histories of Q factor, mode volume and wavelength. Figs. 25 and 26 show the optimal configuration, the distribution of the electric energy density $\epsilon|E|^2$ and the electric field intensity $|E|^2$ for each optimization. These figures are shown in the design domain, which is a 1.5 μm × 2 μm box whose left side corresponds to the center axis. The procedure needed 100 and 30 iterations until convergence. The resulting Q factor, mode volume and wavelength are $Q_{rad} = 6.000 \times 10^7$, $V_{mode} = 1.760 \times 10^{-19}$, $\lambda = 1207$ nm and $Q_{rad} = 3.943 \times 10^4$, $V_{mode} = 4.767 \times 10^{-20}$, $\lambda = 1200$ nm in Figs. 25 and 26 respectively. These results are similar to those obtained in [67], although the two-step optimization composed of topology optimization and phase field in [67] differs from the proposed framework. In Fig. 25, the optimal shape has a large smooth convex form covering the electric-field hot spot to reduce radiation losses. In contrast to high-Q-factor

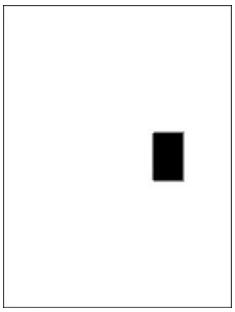

Fig. 23. Initial shapes for designing the dielectric ring resonator.

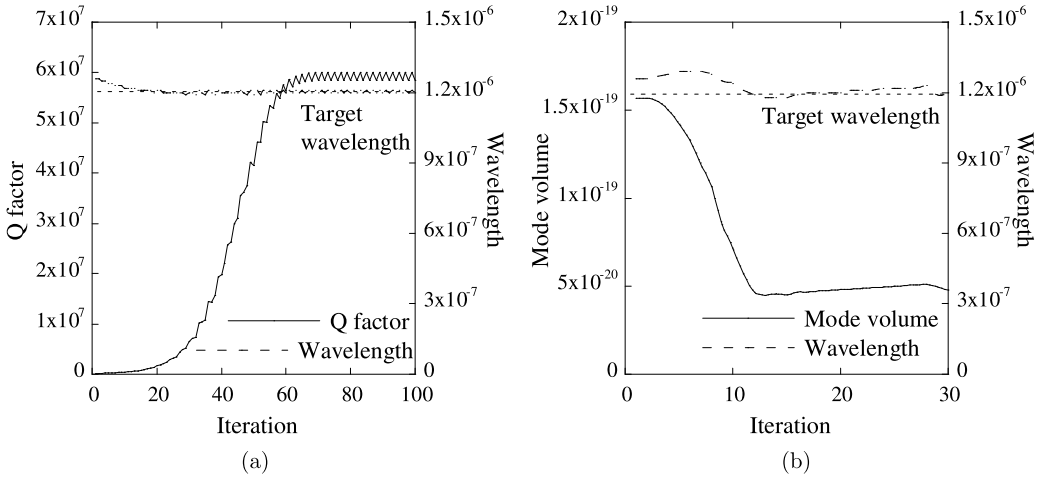

Fig. 24. Convergence history of (a) Q factor, (b) mode volume and wavelength of the dielectric ring resonator optimization.

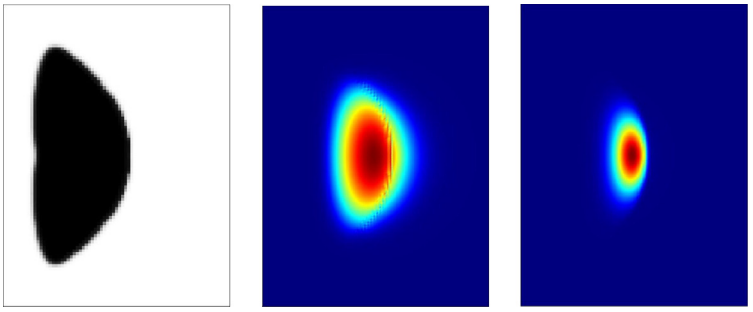

Fig. 25. Optimal shapes obtained by maximizing Q_{rad}. (a) Optimal shape. (b) Electric field intensity $|E|^2$ distribution. (c) Electric energy density $\epsilon|E|^2$ distribution.

shape, the low-mode-volume optimal shape shown in Fig. 26 has a small concave form near the center to enhance the maximum electric energy. The variations of the Q factor and constraint after extracting black and white shapes are 4.49% and 0.00%, respectively, in Fig. 25. The variation of the mode volume and constraint after extracting black and white shapes are 12.15% and 1.67%, respectively, in Fig. 26. Since the center of the optimal configuration is very thin, the density of one element has a large effect on the performance of the shape with optimal mode volume.

6. Conclusion

We have developed the phase field method for shape optimization in the context of designing dielectric devices for electromagnetic wave propagation. The proposed method achieves shape optimization using an implicit domain representation function that accepts the topology change as in the level set method. Comparing with the level set method, our method

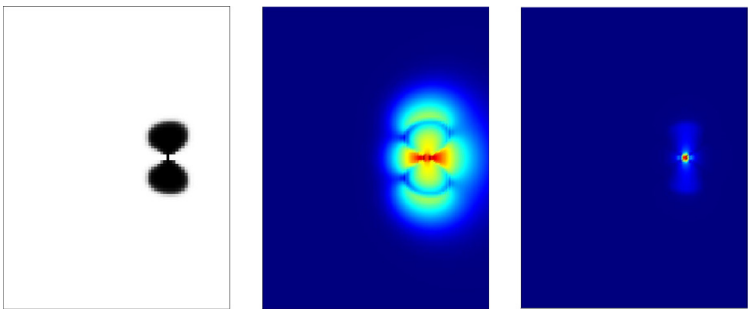

Fig. 26. Optimal shapes obtained by maximizing V_{mode}. (a) Optimal shape. (b) Electric field intensity $|E|^2$ distribution. (c) Electric energy density $\epsilon|E|^2$ distribution.

has an advantage in terms of simplicity, since it does not require extra re-initializing operations of the domain-representing function. We performed four successful optimizations using this method.

The most important advantage of the proposed method is its compatibility with the topology optimization. The domain representation and sensitivity analysis are identical to those of topology optimization in their formulation. Thus, the numerous electromagnetic wave propagation problems studied through topology optimization can be solved with the phase field method. Since the proposed methodology has initial dependency, the optimization can be more effective by generating initial shapes with topology optimization as performed in [67].

The drawback of the phase field method is the thickness of the front domain corresponding to the actual boundary of the object. Thus, errors in shapes and performances are inevitable in the actual and numerical models. We studied the error in each optimization by depicting black and white shapes in the optimal configuration. The error is under about 5% when one element is small enough. However, when it is not, the error becomes large as in the last example. In this case, a finer mesh or adaptive mesh method should be used. However, since the proposed method can generate an optimal shape from a very different one, we can say it has enough performance as the optimization methodology.

Acknowledgements

We would like to thank Prof. Masanobu Haraguchi and Prof. Toshihiro Okamoto at the University of Tokushima for their valuable comments and advice on nano-optical devices.

Appendix A. Sensitivity analysis

We derive the objective functions with respect to the phase field function based on [81]. We use coefficients A and B to represent the Helmholtz equations in general form with respect to the electric field $\boldsymbol{E}$ and the magnetic field $\boldsymbol{H}$:

$$\nabla \times (A\nabla \times \boldsymbol{u}) + B\frac{\omega^2}{c^2}\boldsymbol{u} = 0, \tag{A.1}$$

where $\boldsymbol{u} = \boldsymbol{E}$, $A = 1$ and $B = \epsilon$ for the electric field representation and $\boldsymbol{u} = \boldsymbol{H}$, $A = \frac{1}{\epsilon}$ and $B = 1$ for the magnetic field representation. The weak form of this equation on the domain D and its boundary Γ are represented as

$$a(\boldsymbol{u}, \boldsymbol{v}) - \omega^2 b(\boldsymbol{u}, \boldsymbol{v}) - c(\boldsymbol{u}, \boldsymbol{v}) = 0, \tag{A.2}$$

where

$$a(\boldsymbol{u}, \boldsymbol{v}) = \int_D (\nabla \times \boldsymbol{v}) \cdot (A\nabla \times \boldsymbol{u})\, dx, \tag{A.3}$$

$$b(\boldsymbol{u}, \boldsymbol{v}) = \int_D B\frac{1}{c^2}\boldsymbol{v} \cdot \boldsymbol{u}\, dx, \tag{A.4}$$

$$c(\boldsymbol{u}, \boldsymbol{v}) = \int_\Gamma \boldsymbol{n} \cdot \{\boldsymbol{v} \times (\nabla \times \boldsymbol{u})\}\, ds, \tag{A.5}$$

and $\boldsymbol{v}$ is the test function. When the wave excitation with frequency ω exists, the state equation is solved deterministically with respect to the variable $\boldsymbol{u}$. However, when the eigenfrequency ω is calculated without any wave excitation, the above equation is solved as an eigenvalue problem. In that case, ω^2 and $\boldsymbol{u}$ represent the eigenvalue and the eigenmode respectively.

First, we consider the deterministic problems with wave excitation. The general objective function is defined as the functional on the domain D:

$$J(\phi) = \int_D j(\boldsymbol{u})\, dx. \tag{A.6}$$

The derivative of this function in the direction θ is then

$$\langle J'(\phi), \theta \rangle = \int_D j'(\boldsymbol{u}) \langle \boldsymbol{u}'(\phi), \theta \rangle dx = \int_D j'(\boldsymbol{u}) \boldsymbol{v}\, dx, \tag{A.7}$$

where $\boldsymbol{v} = \langle \boldsymbol{u}'(\phi), \theta \rangle$. Using the state equation and the objective function, and considering the test function of the state equation as the adjoint variable $\boldsymbol{p}$, the Lagrangian is

$$L(\phi, \boldsymbol{u}, \boldsymbol{p}) = \int j(\boldsymbol{u})\, dx + a(\boldsymbol{u}, \boldsymbol{p}) - \omega^2 b(\boldsymbol{u}, \boldsymbol{p}) + c(\boldsymbol{u}, \boldsymbol{p}). \tag{A.8}$$

Using this, the derivative of the objective function can be expressed as

$$\begin{aligned} \langle J'(\phi), \theta \rangle &= \langle L'(\phi), \theta \rangle \\ &= \left\langle \frac{\partial L}{\partial \phi}(\phi, \boldsymbol{u}, \boldsymbol{p}), \theta \right\rangle + \left\langle \frac{\partial L}{\partial \boldsymbol{u}}(\phi, \boldsymbol{u}, \boldsymbol{p}), \langle \boldsymbol{u}'(\phi), \theta \rangle \right\rangle \\ &= \left\langle \frac{\partial L}{\partial \phi}(\phi, \boldsymbol{u}, \boldsymbol{p}), \theta \right\rangle + \left\langle \frac{\partial L}{\partial \boldsymbol{u}}(\phi, \boldsymbol{u}, \boldsymbol{p}), \boldsymbol{v} \right\rangle. \end{aligned} \tag{A.9}$$

Consider the case where the second term is zero. The second term is

$$\left\langle \frac{\partial L}{\partial \boldsymbol{u}}, \boldsymbol{v} \right\rangle = \int j'(\boldsymbol{u}) \boldsymbol{v}\, dx + a(\boldsymbol{v}, \boldsymbol{p}) - \omega^2 b(\boldsymbol{v}, \boldsymbol{p}) - c(\boldsymbol{v}, \boldsymbol{p}) = 0. \tag{A.10}$$

The second term of Eq. (A.9) can be ignored when the adjoint state $\boldsymbol{p}$ satisfies the above adjoint equation. On the other hand, replacing the test function $\boldsymbol{v}$ by the adjoint variable $\boldsymbol{p}$, the derivative of Eq. (A.2) with respect to ϕ in the θ direction is

$$a(\boldsymbol{v}, \boldsymbol{p}) - \omega^2 b(\boldsymbol{v}, \boldsymbol{p}) - c(\boldsymbol{v}, \boldsymbol{p}) + \int_D (\nabla \times \boldsymbol{p}) \cdot \big(A'(\phi) \nabla \times \boldsymbol{u}\big) \theta\, dx - \int_D B'(\phi) \frac{\omega^2}{c^2} \boldsymbol{p} \cdot \boldsymbol{u} \theta\, dx = 0. \tag{A.11}$$

Substituting Eq. (A.11) into Eq. (A.10), we obtain

$$\int j'(\boldsymbol{u}) \boldsymbol{v}\, dx = \int_D (\nabla \times \boldsymbol{p}) \cdot \big(A'(\phi) \nabla \times \boldsymbol{u}\big) \theta\, dx - \int_D B'(\phi) \frac{\omega^2}{c^2} \boldsymbol{p} \cdot \boldsymbol{u} \theta\, dx. \tag{A.12}$$

Substituting Eq. (A.12) into Eq. (A.7), the derivative of the objective function is

$$J'(\phi) = (\nabla \times \boldsymbol{p}) \cdot \big(A'(\phi) \nabla \times \boldsymbol{u}\big) - B'(\phi) \frac{\omega^2}{c^2} \boldsymbol{p} \cdot \boldsymbol{u}. \tag{A.13}$$

Substituting the objective function in Eq. (20), $\boldsymbol{u} = \boldsymbol{E}$, $A = 1$ and $B = \epsilon$ into Eqs. (A.13) and (A.10), we obtain Eqs. (35) and (36). When we use the sensitivity of the S-parameter to the magnetic field $\boldsymbol{H}$ in the objective function in Eq. (26), we use $A = \frac{1}{\epsilon}$ and $B = 1$. When the objective function is S_{12}, we directly obtain Eqs. (39) and (40) by using Eq. (A.13) and substituting Eq. (25) into Eq. (A.10). On the other hand, when the objective function is S_{11}, we obtain an equation similar to the state equation (13) with the boundary condition in Eqs. (16)–(18) obtained by substituting Eq. (24) into Eq. (A.10). This equation represents the response for the incident wave $\boldsymbol{E}^{\mathrm{inc}} / \int_{\Gamma_{\mathrm{in}}} |\boldsymbol{E}_1^{\mathrm{inc}}|^2\, ds$ on the boundary Γ_{in}. The result is calculated by multiplying $1 / \int_{\Gamma_{\mathrm{in}}} |\boldsymbol{E}_1^{\mathrm{inc}}|^2\, ds$ by the state variable. Thus, the sensitivity in Eq. (38) is obtained without calculating the adjoint variable.

Next, we consider the eigenvalue problem without any wave excitation. When the state equation (A.2) is solved to obtain the i-th-order eigenvalue $\Lambda_i = \omega_i^2$ and eigenmode $\boldsymbol{u}_i$, and the objective function is Λ_i, we define the Lagrangian considering the test function of the state equation as the adjoint variable $\boldsymbol{p}$:

$$L(\phi, \boldsymbol{u}_i, \boldsymbol{p}) = \Lambda_i + a(\boldsymbol{u}_i, \boldsymbol{p}) - \Lambda_i b(\boldsymbol{u}_i, \boldsymbol{p}) - c(\boldsymbol{u}_i, \boldsymbol{p}). \tag{A.14}$$

The derivative of L is obtained the same way as with Eq. (A.9). Here, the second term that should become zero is

$$\left\langle \frac{\partial L}{\partial \boldsymbol{u}_i}, \boldsymbol{v} \right\rangle = \left\langle \Lambda_i'(\boldsymbol{u}_i), \boldsymbol{v} \right\rangle \left(1 - b(\boldsymbol{u}_i, \boldsymbol{p})\right) + a(\boldsymbol{v}, \boldsymbol{p}) - \Lambda_i b(\boldsymbol{v}, \boldsymbol{p}) - c(\boldsymbol{v}, \boldsymbol{p}) = 0, \tag{A.15}$$

where $\boldsymbol{v} = \langle \boldsymbol{u}_i'(\phi), \theta \rangle$. Here, when $\boldsymbol{v} = \boldsymbol{p} = \boldsymbol{u}_i$, the right side of the above equation becomes zero. Thus, the optimization of the eigenvalue is self-adjoint. However, the derivative of the eigenvalue in Eq. (A.2) is

$$\begin{aligned} &a(\boldsymbol{v}, \boldsymbol{p}) - \Lambda_i b(\boldsymbol{v}, \boldsymbol{p}) - c(\boldsymbol{v}, \boldsymbol{p}) - \left\langle \Lambda_i'(\phi), \theta \right\rangle b(\boldsymbol{u}_i, p) \\ &\quad + \int_D (\nabla \times \boldsymbol{p}) \cdot \left(A'(\phi) \nabla \times \boldsymbol{u}_i\right) \theta \, dx - \int_D B'(\phi) \frac{\Lambda_i}{c^2} \boldsymbol{p} \cdot \boldsymbol{u}_i \theta \, dx = 0. \end{aligned} \tag{A.16}$$

Substituting $\boldsymbol{p} = \boldsymbol{u}_i$ into the above equation, the sensitivity of the eigenvalue is obtained as

$$\Lambda_i'(\phi) = (\nabla \times \boldsymbol{u}_i) \cdot \left(A'(\phi) \nabla \times \boldsymbol{u}_i\right) - B'(\phi) \frac{\Lambda_i}{c^2} \boldsymbol{u}_i \cdot \boldsymbol{u}_i. \tag{A.17}$$

Substituting $\boldsymbol{u}_i = \boldsymbol{E}_i$, $A = 1$, and $B = \epsilon$ and $\boldsymbol{u}_i = \boldsymbol{H}_i$, $A = \frac{1}{\epsilon}$ and $B = 1$ into Eq. (A.17), the sensitivities in Eqs. (34) and (43) are obtained respectively. Note that when designing the dielectric ring resonator, the operator $c(\boldsymbol{u}, \boldsymbol{v})$ in Eq. (A.2) is replaced by $\int_D p(\nabla \cdot \boldsymbol{p})(\nabla \cdot \boldsymbol{v}) \, dx + \int_\Gamma \boldsymbol{n} \cdot \{\boldsymbol{v} \times (\nabla \times \boldsymbol{u})\} \, ds$ in the derivation. However, the same result is obtained since these terms do not depend on the phase field function ϕ.

We represent the objective function as an eigenmode as follows:

$$J(\phi) = \int_D j(\boldsymbol{u}_i) \, dx. \tag{A.18}$$

The derivative of this function in the θ direction is then

$$\left\langle J'(\phi), \theta \right\rangle = \int_D j'(\boldsymbol{u}_i) \left\langle \boldsymbol{u}_i'(\phi), \theta \right\rangle x \, dx = \int_D j'(\boldsymbol{u}_i) \boldsymbol{v} \, dx. \tag{A.19}$$

The Lagrangian is defined considering the test function of the state equation as the adjoint variable $\boldsymbol{p}$ as follows:

$$L(\phi, \boldsymbol{u}_i, \boldsymbol{p}) = J(\phi) + a(\boldsymbol{u}_i, \boldsymbol{p}) - \Lambda_i b(\boldsymbol{u}_i, \boldsymbol{p}) - c(\boldsymbol{u}_i, \boldsymbol{p}). \tag{A.20}$$

The derivative of L is obtained the same way as with Eq. (A.9). Here, the second term that should become zero is

$$\left\langle \frac{\partial L}{\partial \boldsymbol{u}_i}, \boldsymbol{v} \right\rangle = \int j'(\boldsymbol{u}_i) \boldsymbol{v} \, dx - \left\langle \Lambda_i'(\boldsymbol{u}_i), \boldsymbol{v} \right\rangle b(\boldsymbol{u}_i, \boldsymbol{p}) + a(\boldsymbol{v}, \boldsymbol{p}) - \Lambda_i b(\boldsymbol{v}, \boldsymbol{p}) - c(\boldsymbol{v}, \boldsymbol{p}) = 0. \tag{A.21}$$

The term $\langle \Lambda_i'(\boldsymbol{u}_i), \boldsymbol{v} \rangle$ becomes zero from the eigenvalue definition. Thus, the above equation is simplified as follows:

$$\int j'(\boldsymbol{u}_i) \boldsymbol{v} \, dx + a(\boldsymbol{v}, \boldsymbol{p}) - \Lambda_i b(\boldsymbol{v}, \boldsymbol{p}) - c(\boldsymbol{v}, \boldsymbol{p}) = 0. \tag{A.22}$$

When the adjoint state $\boldsymbol{p}$ satisfies the above adjoint equation, the second term of Eq. (A.9) can be ignored. Substituting Eq. (A.16) into Eq. (A.21), we obtain the following equation:

$$\begin{aligned} &\int j'(\boldsymbol{u}_i) \boldsymbol{v} \, dx - b(\boldsymbol{u}_i, p) \left\{ \int_D (\nabla \times \boldsymbol{u}_i) \cdot \left(A'(\phi) \nabla \times \boldsymbol{u}_i\right) \theta \, dx - \int_D B'(\phi) \frac{\Lambda_i}{c^2} \boldsymbol{u}_i \cdot \boldsymbol{u}_i \theta \, dx \right\} \\ &\quad + \int_D (\nabla \times \boldsymbol{p}) \cdot \left(A'(\phi) \nabla \times \boldsymbol{u}_i\right) \theta \, dx - \int_D B'(\phi) \frac{\Lambda_i}{c^2} \boldsymbol{p} \cdot \boldsymbol{u}_i \theta \, dx = 0. \end{aligned} \tag{A.23}$$

Substituting Eq. (A.23) into Eq. (A.19), the derivative of the objective function is

$$\begin{aligned} J'(\phi) = &-b(\boldsymbol{u}_i, \boldsymbol{p}) \left\{ (\nabla \times \boldsymbol{u}_i) \cdot \left(A'(\phi) \nabla \times \boldsymbol{u}_i\right) - B'(\phi) \frac{\Lambda_i}{c^2} \boldsymbol{u}_i \cdot \boldsymbol{u}_i \right\} \\ &+ (\nabla \times \boldsymbol{u}_i) \cdot \left(A'(\phi) \nabla \times \boldsymbol{p}\right) - B'(\phi) \frac{\Lambda_i}{c^2} \boldsymbol{u}_i \cdot \boldsymbol{p}. \end{aligned} \tag{A.24}$$

Substituting the objective function in Eq. (32), $\boldsymbol{u}_i = \boldsymbol{H}_i$, $A = \frac{1}{\epsilon}$ and $B = 1$ into Eq. (A.24) and Eq. (A.22) and replacing the operator $c(\boldsymbol{u}, \boldsymbol{v})$ by $\int_D p(\nabla \cdot \boldsymbol{p})(\nabla \cdot \boldsymbol{v}) \, dx + \int_\Gamma \boldsymbol{n} \cdot \{\boldsymbol{v} \times (\nabla \times \boldsymbol{u})\} \, ds$, we obtain Eqs. (45) and (46).

References

[1] S.J. Cox, D.C. Dobson, Band structure optimization of two-dimensional photonic crystals in h-polarization, J. Comput. Phys. 158 (2) (2000) 214–224.
[2] J. Jensen, O. Sigmund, Systematic design of photonic crystal structures using topology optimization: Low-loss waveguide bends, Appl. Phys. Lett. 84 (12) (2004) 2022–2024.
[3] W.R. Frei, D.A. Tortorelli, H.T. Johnson, Topology optimization of a photonic crystal waveguide termination to maximize directional emission, Appl. Phys. Lett. 86 (2005) 111114.
[4] C.Y. Kao, S. Osher, E. Yablonovitch, Maximizing band gaps in two-dimensional photonic crystals by using level set methods, Appl. Phys. B, Lasers Opt. 81 (2) (2005) 235–244.
[5] O. Sigmund, K.G. Hougaard, Geometric properties of optimal photonic crystals, Phys. Rev. Lett. 100 (15) (2008) 153904.
[6] J. Andkjær, S. Nishiwaki, T. Nomura, O. Sigmund, Topology optimization of grating couplers for the efficient excitation of surface plasmons, J. Opt. Soc. Am. B 27 (9) (2010) 1828–1832.
[7] A.R. Diaz, O. Sigmund, A topology optimization method for design of negative permeability metamaterials, Struct. Multidiscip. Optim. 41 (2) (2010) 163–177.
[8] S.W. Zhou, W. Li, G.Y. Sun, Q. Li, A level-set procedure for the design of electromagnetic metamaterials, Opt. Express 18 (7) (2010) 6693–6702.
[9] C. Rupp, M. Dunn, K. Maute, Switchable phononic wave filtering, guiding, harvesting, and actuating in polarization-patterned piezoelectric solids, Appl. Phys. Lett. 96 (2010) 111902.
[10] J. Andkjær, O. Sigmund, Topology optimized low-contrast all-dielectric optical cloak, Appl. Phys. Lett. 98 (2) (2011) 021112.
[11] J.S. Jensen, O. Sigmund, Topology optimization for nano-photonics, Laser Photonics Rev. 5 (2) (2011) 308–321.
[12] M.P. Bendsøe, N. Kikuchi, Generating optimal topologies in structural design using a homogenization method, Comput. Methods Appl. Mech. Eng. 71 (2) (1988) 197–224.
[13] G. Allaire, Shape Optimization by the Homogenization Method, Springer-Verlag, New York, 2001.
[14] M.P. Bendsøe, O. Sigmund, Topology Optimization: Theory, Methods, and Applications, Springer-Verlag, Berlin, 2003.
[15] J.A. Sethian, A. Wiegmann, Structural boundary design via level set and immersed interface methods, J. Comput. Phys. 163 (2) (2000) 489–528.
[16] S.J. Osher, F. Santosa, Level set methods for optimization problems involving geometry and constraints. I. Frequencies of a two-density inhomogeneous drum, J. Comput. Phys. 171 (2001) 272–288.
[17] M.Y. Wang, X. Wang, D. Guo, A level set method for structural topology optimization, Comput. Methods Appl. Mech. Eng. 192 (1–2) (2003) 227–246.
[18] G. Allaire, F. Jouve, A.M. Toader, Structural optimization using sensitivity analysis and a level-set method, J. Comput. Phys. 194 (1) (2004) 363–393.
[19] O. Pironneau, Optimal Shape Design for Elliptic Systems, Springer-Verlag, New York, 1984.
[20] J. Sokołowski, J.P. Zolesio, Introduction to Shape Optimization: Shape Sensitivity Analysis, Springer-Verlag, Berlin, 1992.
[21] S. Osher, J.A. Sethian, Fronts propagating with curvature-dependent speed: Algorithms based on Hamilton–Jacobi formulations, J. Comput. Phys. 79 (1988) 12–49.
[22] J.A. Sethian, Level Set Methods and Fast Marching Methods, Cambridge University Press, New York, 1999.
[23] S. Osher, R.P. Fedkiw, Level Set Methods and Dynamic Implicit Surfaces, Springer, New York, 2003.
[24] Y.G. Chen, Y. Giga, S. Goto, Uniqueness and existence of viscosity solutions of generalized mean curvature flow equations, J. Differ. Geom. 33 (3) (1991) 749–786.
[25] L.C. Evans, J. Spruck, Motion of level sets by mean curvature I, J. Differ. Geom. 33 (3) (1991) 635–681.
[26] Y. Giga, Surface Evolution Equations: A Level Set Approach, Birkhäuser, Basel, 2006.
[27] G. Allaire, F. Jouve, A level-set method for vibration and multiple loads structural optimization, Comput. Methods Appl. Mech. Eng. 194 (30–33) (2005) 3269–3290.
[28] Z. Luo, L. Tong, M.Y. Wang, S. Wang, Shape and topology optimization of compliant mechanisms using a parameterization level set method, J. Comput. Phys. 227 (1) (2007) 680–705.
[29] F. de Gournay, G. Allaire, F. Jouve, Shape and topology optimization of the robust compliance via the level set method, ESAIM Control Optim. Calc. Var. 14 (1) (2008) 43–70.
[30] S. Zhou, Q. Li, A variational level set method for the topology optimization of steady-state Navier–Stokes flow, J. Comput. Phys. 227 (24) (2008) 10178–10195.
[31] Z. Luo, L. Tong, H. Ma, Shape and topology optimization for electrothermomechanical microactuators using level set methods, J. Comput. Phys. 228 (9) (2009) 3173–3181.
[32] S. Zhou, W. Li, Q. Li, Level-set based topology optimization for electromagnetic dipole antenna design, J. Comput. Phys. 229 (19) (2010) 6915–6930.
[33] G. Allaire, F. Jouve, N. Van Goethem, Damage and fracture evolution in brittle materials by shape optimization methods, J. Comput. Phys. 230 (12) (2011) 5010–5044.
[34] S. Yamasaki, T. Nomura, A. Kawamoto, K. Sato, S. Nishiwaki, A level set-based topology optimization method targeting metallic waveguide design problems, Int. J. Numer. Methods Eng. 87 (9) (2011) 844–868.
[35] S.W. Zhou, W. Li, G.Y. Sun, Q. Li, A level-set procedure for the design of electromagnetic metamaterials, Opt. Express 18 (7) (2010) 6693–6702.
[36] S.W. Zhou, W. Li, Y. Chen, G.Y. Sun, Q. Li, Topology optimization for negative permeability metamaterials using level-set algorithm, Acta Mater. 59 (7) (2011) 2624–2636.
[37] S. Yamasaki, T. Nomura, K. Sato, N. Michishita, Y. Yamada, A. Kawamoto, Level set-based topology optimization targeting dielectric resonator-based composite right- and left-handed transmission lines, Int. J. Numer. Methods Eng. 89 (2012) 1272–1295.
[38] J.W. Cahn, J.E. Hilliard, Free energy of a nonuniform system. I. Interfacial free energy, J. Chem. Phys. 28 (1958) 258–267.
[39] S.M. Allen, J.W. Cahn, A microscopic theory for antiphase boundary motion and its application to antiphase domain coarsening, Acta Metall. 27 (1979) 1085–1095.
[40] G. Fix, Phase field models for free boundary problems, in: A. Fasano, M. Primicerio (Eds.), Free Boundary Problems, Theory and Application, Pitman, New York, 1983, pp. 580–589.
[41] J.B. Collins, H. Levine, Diffuse interface model of diffusion-limited crystal growth, Phys. Rev. B 31 (9) (1985) 6119–6122.
[42] G. Caginalp, An analysis of a phase field model of a free boundary, Arch. Ration. Mech. Anal. 92 (3) (1986) 205–245.
[43] R. Kobayashi, Modeling and numerical simulations of dendritic crystal growth, Physica D 63 (3–4) (1993) 410–423.
[44] S. Wang, R. Sekerka, A. Wheeler, B. Murray, S. Coriell, R. Braun, G. McFadden, Thermodynamically-consistent phase-field models for solidification, Physica D 69 (1–2) (1993) 189–200.
[45] W.J. Boettinger, J.A. Warren, C. Beckermann, A. Karma, Phase-field simulation of solidification, Annu. Rev. Mater. Res. 32 (2002) 163–194.
[46] L.Q. Chen, Phase-field models for microstructure evolution, Annu. Rev. Mater. Res. 32 (2002) 113–140.
[47] G.B. Macfadden, Phase-field models of solidification, Contemp. Math. 306 (2002) 107–145.
[48] B. Bourdin, A. Chambolle, Design-dependent loads in topology optimization, ESAIM Control Optim. Calc. Var. 9 (2003) 19–48.
[49] L. Ambrosio, G. Buttazzo, An optimal design problem with perimeter penalization, Calc. Var. 1 (1993) 55–69.
[50] R.B. Haber, C.S. Jog, M.P. Bendsøe, A new approach to variable-topology shape design using a constraint on perimeter, Struct. Optim. 11 (1) (1996) 1–12.

[51] M. Burger, R. Stainko, Phase-field relaxation of topology optimization with local stress constraints, SIAM J. Control Optim. 45 (4) (2006) 1447–1466.
[52] S. Zhou, M. Wang, Multimaterial structural topology optimization with a generalized Cahn–Hilliard model of multiphase transition, Struct. Multidiscip. Optim. 33 (2) (2007) 89–111.
[53] M. Wallin, M. Ristinmaa, H. Askfelt, Optimal topologies derived from a phase-field method, Struct. Multidiscip. Optim. (2011) 1–13.
[54] L. Blank, H. Garcke, L. Sarbu, T. Srisupattarawanit, V. Styles, A. Voigt, Phase-field approaches to structural topology optimization, in: Constrained Optimization and Optimal Control for Partial Differential Equations, Springer, 2012, pp. 245–256.
[55] A. Takezawa, S. Nishiwaki, M. Kitamura, Shape and topology optimization based on the phasefield method and sensitivity analysis, J. Comput. Phys. 229 (7) (2010) 2697–2718.
[56] A.L. Gain, G.H. Paulino, Phase-field based topology optimization with polygonal elements: A finite volume approach for the evolution equation, Struct. Multidiscip. Optim. 46 (3) (2012) 327–342.
[57] G. Barles, H.M. Soner, P.E. Souganidis, Front propagation and phase field theory, SIAM J. Control Optim. 31 (1993) 439–469.
[58] P. Fife, Dynamics of Internal Layers and Diffusive Interfaces, SIAM, Philadelphia, 1988.
[59] J. Rubinstein, P. Sternberg, J.B. Keller, Fast reaction, slow diffusion, and curve shortening, SIAM J. Appl. Math. 49 (1989) 116–133.
[60] J.D. Joannopoulos, S.G. Johnson, J.N. Winn, R.D. Meade, Photonic Crystals: Molding the Flow of Light, second edition, Princeton University Press, Princeton, 2008.
[61] S.J. Cox, D.C. Dobson, Maximizing band gaps in two-dimensional photonic crystals, SIAM J. Appl. Math. 59 (6) (1999) 2108–2120.
[62] M. Otomori, T. Yamada, K. Izui, S. Nishiwaki, J. Andkjær, A topology optimization method based on the level set method for the design of negative permeability dielectric metamaterials, Comput. Methods Appl. Mech. Eng. 237–240 (2012) 192–211.
[63] S. O'Brien, J.B. Pendry, Photonic band-gap effects and magnetic activity in dielectric composites, J. Phys. Condens. Matter 14 (2002) 4035–4044.
[64] L. Peng, L. Ran, H. Chen, H. Zhang, J.A. Kong, T.M. Grzegorczyk, Experimental observation of left-handed behavior in an array of standard dielectric resonators, Phys. Rev. Lett. 98 (15) (2007) 157403.
[65] Q. Zhao, J. Zhou, F. Zhang, D. Lippens, Mie resonance-based dielectric metamaterials, Mater. Today 12 (12) (2009) 60–69.
[66] D.R. Smith, D.C. Vier, T. Koschny, C.M. Soukoulis, Electromagnetic parameter retrieval from inhomogeneous metamaterials, Phys. Rev. E 71 (3) (2005) 036617.
[67] A. Takezawa, M. Kitamura, Cross-sectional shape optimization of whispering-gallery ring resonators, J. Lightwave Technol. 30 (17) (2012) 2776–2782.
[68] S. McCall, A. Levi, R. Slusher, S. Pearton, R. Logan, Whispering-gallery mode microdisk lasers, Appl. Phys. Lett. 60 (3) (1992) 289–291.
[69] A. Oraevsky, Whispering-gallery waves, Quantum Electron. 32 (5) (2002) 377–400.
[70] K.J. Vahala, Optical microcavities, Nature 424 (2003) 839–846.
[71] M. Koshiba, K. Hayata, M. Suzuki, Improved finite-element formulation in terms of the magnetic field vector for dielectric waveguides, IEEE Trans. Microw. Theory Tech. 33 (3) (1985) 227–233.
[72] M. Oxborrow, Traceable 2-D finite-element simulation of the whispering-gallery modes of axisymmetric electromagnetic resonators, IEEE Trans. Microw. Theory Tech. 55 (6) (2007) 1209–1218.
[73] K. Srinivasan, M. Borselli, O. Painter, A. Stintz, S. Krishna, Cavity Q, mode volume, and lasing threshold in small diameter AlGaAs microdisks with embedded quantum dots, Opt. Express 14 (3) (2006) 1094–1105.
[74] D.W. Prather, S. Shi, A. Sharkawy, J. Murakowski, G.J. Schneider, Photonic Crystals, Theory, Applications and Fabrication, Wiley, Hoboken, 2009.
[75] S.H. Gould, Variational Methods for Eigenvalue Problems: An Introduction to the Methods of Rayleigh, Ritz, Weinstein, and Aronszajn, Dover Publications, New York, 1995.
[76] G. Allaire, Numerical Analysis and Optimization: An Introduction to Mathematical Modelling and Numerical Simulation, Oxford University Press, 2007.
[77] E.J. Haug, K.K. Choi, V. Komkov, Design Sensitivity Analysis of Structural Systems, Academic Press, Orlando, 1986.
[78] A.P. Seyranian, E. Lund, N. Olhoff, Multiple eigenvalues in structural optimization problems, Struct. Optim. 8 (4) (1994) 207–227.
[79] J.A. Warren, R. Kobayashi, A.E. Lobkovsky, W. Craig Carter, Extending phase field models of solidification to polycrystalline materials, Acta Mater. 51 (20) (2003) 6035–6058.
[80] T.S. Kim, Y.Y. Kim, Mac-based mode-tracking in structural topology optimization, Comput. Struct. 74 (3) (2000) 375–383.
[81] G. Allaire, Conception optimale de structures, Springer-Verlag, Berlin, 2007.